Cellular and Molecular Life Sciences (2022) 79:540
https://doi.org/10.1007/s00018-022-04506-9

ORIGINAL ARTICLE

Hetero-pentamerization determines mobility and conductance of Glycine receptor α3 splice variants

Veerle Lemmens[1,2] · Bart Thevelein[1] · Yana Vella[6] · Svenja Kankowski[3,4] · Julia Leonhard[4] · Hideaki Mizuno[5] · Susana Rocha[2] · Bert Brône[6] · Jochen C. Meier[4] · Jelle Hendrix[1,2]

Received: 1 April 2022 / Revised: 21 July 2022 / Accepted: 23 July 2022

Abstract

Glycine receptors (GlyRs) are ligand-gated pentameric chloride channels in the central nervous system. GlyR-α3 is a possible target for chronic pain treatment and temporal lobe epilepsy. Alternative splicing into K or L variants determines the subcellular fate and function of GlyR-α3, yet it remains to be shown whether its different splice variants can functionally co-assemble, and what the properties of such heteropentamers would be. Here, we subjected GlyR-α3 to a combined fluorescence microscopy and electrophysiology analysis. We employ masked Pearson's and dual-color spatiotemporal correlation analysis to prove that GlyR-α3 splice variants heteropentamerize, adopting the mobility of the K variant. Fluorescence-based single-subunit counting experiments revealed a variable and concentration ratio dependent hetero-stoichiometry. Via cell-attached single-channel electrophysiology we show that heteropentamers exhibit currents in between those of K and L variants. Our data are compatible with a model where α3 heteropentamerization fine-tunes mobility and activity of GlyR-α3 channels, which is important to understand and tackle α3 related diseases.

Keywords Glycine receptors · Ligand gated ion channels · Image correlation spectroscopy · Single-molecule fluorescence · Pearson's correlation coefficient · Subunit counting · Protein co-assembly · Diffusion · Stoichiometry · Electrophysiology · Patch clamp

Veerle Lemmens and Bart Thevelein contributed equally to this work.

✉ Jochen C. Meier
jochen.meier@tu-braunschweig.de

Jelle Hendrix
Jelle.hendrix@uhasselt.be

1 Dynamic Bioimaging Lab, Advanced Optical Microscopy Centre and Biomedical Research Institute, Hasselt University, Agoralaan C (BIOMED), 3590 Diepenbeek, Belgium

2 Molecular Imaging and Photonics, Chemistry Department, KU Leuven, 3001 Heverlee, Belgium

3 Institute of Neuroanatomy and Cell Biology, Hannover Medical School, 30625 Hannover, Germany

4 Division Cell Physiology, Zoological Institute, Technical University Braunschweig, 38106 Brunswick, Germany

5 Laboratory of Biomolecular Network Dynamics, Biochemistry, Molecular and Structural Biology Division, Department of Chemistry, KU Leuven, 3001 Heverlee, Belgium

6 Neurophysiology Lab, Biomedical Research Institute, UHasselt, 3590 Diepenbeek, Belgium

Introduction

Neuronal communication in the central nervous system (CNS) is fine-tuned via ionotropic channel proteins such as glycine receptors (GlyRs). Belonging to the family of pentameric ligand-gated ion channels (pLGICs), GlyRs help regulate motor coordination and sensory signal processing [1, 2]. In humans, GlyRs are expressed as one of three α isoforms (α1–3) that heteropentamerize with the β isoform if the latter is present. In this paper we focus on the α3 isoform of GlyR, which in the human body is found in the spinal cord dorsal horn, the brain stem and the hippocampus [3]. In addition, high RNA levels were also found in the cerebral cortex, the amygdala and in the pituitary gland [4]. It is involved in temporal lobe epilepsy (TLE) [5–8] and, due to its crucial involvement in inflammatory pain perception, it is a potential target for chronic pain treatment [9]. Because of its specific localization in the CNS, targeting α3 could lead to reduced side effects compared to other GlyR-α isoforms.

GlyR-α3 is produced as one of two possible splice variants, α3K or α3L. Post-transcriptional exclusion of exon 8

Published online: 05 October 2022

from the GlyR-α3 coding mRNA [3, 10–12] results in the α3K variant lacking 15 amino acids (TEAFALEKFYRF-SDT) in the large intracellular loop between transmembrane α-helices TM3 and TM4 (Fig. 1A). GlyR-α3L is the predominant variant in a healthy brain, outweighing α3K approximately five-fold. Although both variants are always co-expressed in neurons, GlyR-α3K primarily localizes somatodendritically [5, 8, 13, 14], while α3L mostly localizes at the presynapse due to interaction with vesicular trafficking factor SEC8 [8], where it stimulates neurotransmitter release [8, 15–17], similar to other presynaptic chloride channels. Finally, neuronal cells additionally co-expressing GlyR-β endogenously will also contain postsynaptic heteropentameric α–β GlyRs, due to interaction with the postsynaptic scaffold protein gephyrin [18, 19].

Previous reports have used fluorescence microscopy and electrophysiology to investigate the properties of homomeric GlyR-α3. Apart from their overall subcellular localization, fluorescence fluctuation imaging and single-particle tracking revealed that in live cells both (immunostained HA-tagged) splice variants exhibited free and confined diffusion in the membrane. Both fast (apparent diffusion constant $D \sim 0.1$ $\mu m^2/s$) and slow-diffusing ($D \sim 0.01$ $\mu m^2/s$) species could be observed for both variants, with slow and confined diffusion being more prevalent for α3L than α3K [20, 21]. Fluorescence imaging using primary spinal cord or hippocampal neurons, or HEK293 cell lines, also evidenced that α3L is more prone to clustering in the cell membrane [5, 22, 23]. This suggests a role for the insert in the intracellular loop in directly promoting pentamer–pentamer interactions, whether or not combined with linking to immobile submembranous components that enhance the clustering process. It has also been shown using cell culture based whole-cell patch clamp experiments that, overall, α3L expressing cells exhibit

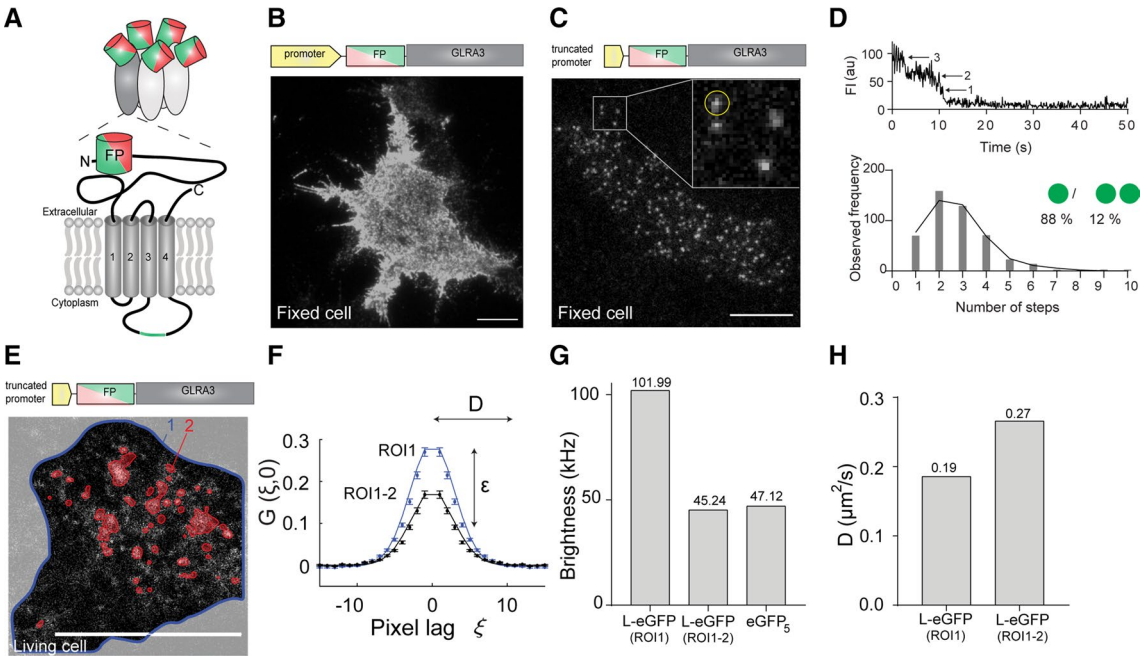

Fig. 1 Low copy number imaging of GlyR-α3L-FP in HEK293 cells allows quantifying single pentamer properties. **A** Subunit structure of GlyR-α3-FP with the fluorescent protein eGFP or mCherry (FP) fused to the terminus of the extracellular N-terminal domain and the position of the TM3-TM4 loop insert for GlyR-α3L in green. **B** Representative cell with high copy number GlyR expression from a plasmid with a stong promoter. Scale bar, 10 µm. **C** Representative fixed cell with low copy number GlyR expression using a plasmid with a truncated promoter. Scale bar, 10 µm. The inset is a magnification of the area indicated by the white square, white spots indicate single receptors, the yellow circle corresponds to the data in the upper part of panel (**D**). **D** Step-wise photobleaching subunit counting identify low numbers of fluorescent eGFP per fluorescent spot in the low copy number cells. **E** Confocal fluorescence image of a live cell expressing GlyR used for raster image correlation spectroscopy (RICS) analysis. The edge of the cell is outlined in blue (region of interest, ROI1) and the high-intensity clusters, automatically selected via frame-to-frame intensity thresholding (see Materials and Methods for more details), are highlighted in red (ROI2). Scale bar, 10 µm. **F** The 1D section of the average 2D RICS autocorrelation function (the reader is referred to Fig. S4A–B for images of the 2D correlation functions) at spatial lag (ξ, 0) of a confocal image series of GlyR-α3L-eGFP expressing cells using either all pixels within ROI1 or within ROI1 minus ROI2. The reader is also referred to Video S1–2 for the different ROIs. The mean brightness ε and mean diffusion constant are determined from the amplitude and shape of the correlation function, respectively. **G** Representative example of the molecular brightness (in kHz/second or kphotons/second) of diffusing GlyR-α3L-eGFP assemblies within ROI1 or within ROI1 minus ROI2, and, as a reference, molecular brightness of diffusing cytosolic $eGFP_5$ measured as close to the bottom membrane as possible. **H** Representative example of the diffusion constant of diffusing GlyR-α3L-eGFP within ROI1 or within ROI1 minus ROI2

slower desensitization kinetics than α3K [3, 24]. Finally, main-state single-channel conductances of 63–105 pS were observed for the α3L variant by different groups [25–29]. For the α3K variant, one group reported a similar conductance of 69 pS, suggesting the TM3-TM4 loop does not contribute to regulating the ion flux through the open channel [25]. However, when several basic residues in the TM3-TM4 loop of the α1 receptor were changed to negatively charged residues, changes in conductance were observed [30].

Besides the molecular and functional differences of the α3 homomers described above, it is intriguing to know whether the two α3 splice variants can also form heteropentamers, and if they do, which effects this would have on GlyR function. Indeed, the pathological effect of the increased K-to-L expression ratio in TLE patients with a severe course of the disease could result from a mere changed concentration balance of K and L homopentamers [5]. Yet, because a changed heterostoichiometry balance of the K/L population might be as, or even more, detrimental (depending on the properties of such heteropentamers), we hypothesize that heteropentamers exist and are functionally different than homopentamers. The existence of α3L/K heteropentamers in HEK293 cells was already suggested [22] via co-localization analysis of the differently labeled splice variants, although in this report the distinction between clusters of overlapping homopentamers or actual heteropentamers could not be made.

In this paper, we hypothesized that GlyR-α3 K/L splice variants functionally interact. If so, we would like to know what the molecular and functional properties of such heteropentamers were. We first developed strategies for expressing and imaging single GlyR-α3 pentamers in the membrane of live cells. We then used a combination of different quantitative fluorescence microscopy imaging and analysis methods including Pearson's co-localization, raster/temporal image correlation spectroscopy [31, 32] and subunit counting via stepwise photobleaching [33, 34] to investigate the mobility, heteropentamerization and heterostoichiometry of co-expressed GlyR-α3 K/L splice variants. Then, we subjected GlyR-α3 expressing cells to functional analysis via single-channel patch clamp.

Results

Advanced methodology for imaging single-pentamer properties of glycine receptors

Physiologically, GlyR-α3 molecules are present both as single pentamers and clusters of pentamers. As we were specifically interested in single pentamers, we first developed a cell-based fluorescent GlyR expression system and an analysis methodology that allows specifically analyzing the molecular properties of single GlyR-α3 pentamers in a way that is unbiased by clusters. First, to visualize the α3L and α3K isoforms of GlyR, we used plasmids encoding the GlyR N-terminally tagged with a green (eGFP) or red (mCherry) fluorescent protein (FP) (Fig. 1A) and transiently transfected these in HEK293 cells. These do not express GlyR endogenously but are known to be a relevant model system for studying GlyRs [3]. Immunocytochemistry (Fig. S1) and whole-cell patch-clamp electrophysiology (Fig. S2-3) confirmed the subcellular distribution and activity, respectively, of the FP-tagged receptors as described recently [5, 35, 36].

Then, we followed a three-pronged approach to achieve the required low (single-molecule) and intermediate (10–100 nM) expression levels that are ideally suited for the planned single-pentamer analyses and for the diffusion analysis, respectively. We truncated the CMV promotor (similar to [37]), reduced the amount of GlyR encoding plasmid DNA while retaining the transfection efficiency via co-transfection with a non-coding plasmid [38] and limited the time between transfection and fixation or live-cell imaging. Using total internal reflection fluorescence microscopy (TIRFM) we imaged fixed cells expressing the normal- or low-expressing GlyR-α3L-eGFP plasmids (Fig. 1B, C). Indeed, with the latter plasmids we could easily find cells that clearly exhibited individual diffraction limited fluorescent spots (Fig. 1C), presumably single pentamers.

We next set out to prove whether these spots corresponded to single GlyR pentamers by recording time-lapse fluorescence images of transiently transfected cells and counting the number of eGFP molecules per diffraction-limited spot using single-spot photobleaching step measurements (Fig. 1D, top). As can be seen from the frequency distribution of the number of steps, a variety of bleaching steps ranging from 1 to 10 was observed (Fig. 1D, bottom). This has been observed before in bleaching experiments of GlyR-α1 in HEK293 cells [33, 39] and is attributed to a mixture of incomplete maturation of the fluorescent proteins, prebleaching of the eGFP, and single pentamers that are overlapping at a spatial scale smaller than the optical resolution. To analyze the data quantitatively, we fitted the distribution to a binomial model (Eq. 1, see "Materials and methods"). This analysis resulted in a probability of 47% for eGFP to be maturated and unbleached and in 88% of spots not overlapping with other spots. Both of these values are similar to previous experiments on GlyR-α1 in HEK293 cells [33, 39]. This experiment thus suggests that in the low-expressing HEK293 cells, about 88% of detected fluorescent spots were likely single pentamers.

Finally, to corroborate that the majority of GlyRs detected in the cell membrane were indeed single pentamers, we used confocal raster image correlation spectroscopy (RICS). Practically, we performed experiments in cells with intermediate expression levels of GlyR-α3L-eGFP (ideally 10–100 nM [40]) (Fig. 1E). In such cells, we observed both regions with

diffuse fluorescence, as well as regions with high-intensity fluorescent clusters, the latter presumably being GlyR aggregates that have been observed before [20]. After spatial autocorrelation of the images (Eq. 5) and fitting the resulting data to Eq. 6, we obtained both the molecular brightness ε (Eq. 7) and the mobility (apparent diffusion constant, *D*) of the GlyR complexes diffusing in the membrane (Fig. 1F). The ε informs on the average number of fluorescing eGFP moieties in the diffusing complexes and, via comparison with a control protein, can be used to assess their average stoichiometry. The *D*, on the other hand, reports on the average size of these diffusing complexes, with slower diffusion indicative of larger complexes. When we included all pixels belonging to the cell membrane into the analysis (ROI1 in Fig. 1E, Fig. S4A and Video S1), the ε that we measured was significantly higher than that of a control protein, a cytosolic tandem eGFP pentamer ($eGFP_5$) that we measured as close to the cell membrane as possible (Fig. 1G). When we additionally excluded the regions with an intense fluorescence signal (ROI1 minus ROI2 in Fig. 1E, Fig. S4B and Video S2), the brightness ε of the diffusing GlyR complexes was indistinguishable from that of the $eGFP_5$ control Fig. 1G. Additionally, this experiment seems to show that properties of single GlyR pentamers can be specifically studied, in the case of intermediate-expression cells, by masking out regions containing clusters. The observed apparent diffusion constant also depended on the ROI that was selected for the RICS analysis. Indeed, diffusion analysis in 'ROI1 minus ROI2' resulted in overall increased mobility, which directly proves the masking procedure efficiently removed the high-stoichiometry GlyR clusters (Fig. 1H).

In summary, we generated HEK293 cells expressing low amounts of GlyR-α3 splice variants labeled with fluorescent proteins and validated single-molecule and fluctuation imaging tools that allow focusing on the properties of single pentameric complexes excluding GlyR clusters. In the rest of the paper all analyses were performed on single GlyR pentamers, unless explicitly stated otherwise. Specifically, we took a closer look at the two splice variants, and at what happened when they are co-expressed in cells.

Single homopentameric K and L variants exhibit a different diffusion signature

As a follow-up of the work of Notelaers et al. [20, 21], we next investigated the mobility of the two different splice variants GlyR-α3L-eGFP and GlyR-α3K-eGFP with RICS [41, 42] and temporal image correlation spectroscopy (TICS) [43], using image masking to specifically focus on single pentamers. RICS, which analyses µs-ms intensity fluctuations occurring within confocal image frames, is typically used to quantify the mobility of faster protein populations ($D \approx 0.1$–$500\ \mu m^2/s$) while TICS, in which tens-of-milliseconds camera pixel intensity fluctuations are correlated over time, is typically used to quantify the mobility of proteins diffusing on a relatively slow timescale ($D \approx 0.001$–$0.1\ \mu m^2/s$). Parallel application of both techniques allows identifying and characterizing different possible mobile protein populations [44]. Essential to this is choosing imaging conditions suited to the type of diffusion process (for RICS, see [45], for TICS, see [46]).

For RICS, we acquired confocal image series of living cells expressing either GlyR-α3L-eGFP or GlyR-α3K-eGFP at 37 °C as illustrated in Fig. 2A. Because in confocal microscopy the laser scans pixel per pixel and line per line while proteins diffuse, the resulting image will contain spatial fluorescence intensity fluctuations along any direction in the image, as depicted in Fig. 2B along the direction of a single line scan. We spatially correlated each image frame in the series (Eq. 5) and via fitting of the average spatial autocorrelation function (Fig. 2C–D, Eq. 6), we determined that the diffusion constants *D* of GlyR-α3L-eGFP ($D = 0.26 \pm 0.11\ \mu m^2/s$) and GlyR-α3K-eGFP ($D = 0.29 \pm 0.08\ \mu m^2/s$) were within experimental error the same (Fig. 2E). At least within the timescale of a single RICS image frame, the K and L variants thus exhibit similar diffusion.

For TICS, time-lapse images were acquired using TIRF-based widefield microscopy in living cells at room temperature (Fig. 2F). As the frame rate using a camera is much faster than for confocal microscopy, and oftentimes similar to the time it takes molecules to diffuse in and out of image pixels, fluorescence intensities tend to fluctuate from frame to frame due to molecular diffusion, as illustrated in Fig. 2G. By temporally autocorrelating each pixel's fluorescence time trace (Eq. 10) and fitting a model to the obtained mean temporal autocorrelation function (Fig. 2H, Eq. 11), the diffusion constant can likewise be determined. In this way we obtained a diffusion constant of $D = 0.089 \pm 0.023\ \mu m^2/s$ for GlyR-α3K-eGFP and a significantly lower diffusion constant of $D = 0.057 \pm 0.014\ \mu m^2/s$ for GlyR-α3L-eGFP (Fig. 1I). First, this analysis reveals a second diffusive GlyR species, as values for *D* were significantly lower as observed with RICS, even when RICS measurement were performed at RT (Fig. S4F). More interestingly, however, the slower component of the L variant is significantly lower than the slow component of the K variant. To investigate the possibility that this could be related to inefficient removal of clusters from the analysis, which would affect the clustering-prone L variant more than the K variant, and thus also the observed mobility (Fig. S4C) [5, 22, 23], we performed a detailed comparison of different masking procedures (Fig. S4D). This showed a dependence of the observed *D* for both K and L on the type of mask used: whole cell (Video S3), static mask (Video S4, mask calculated on the average of all frames), dynamic mask (Video S5, calculated per frame),

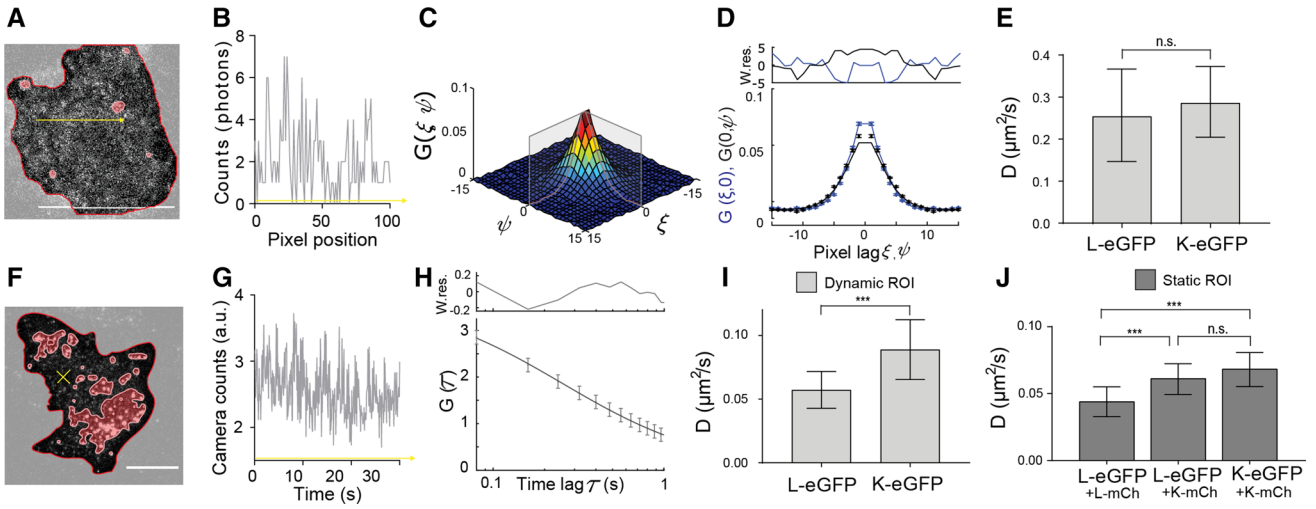

Fig. 2 RICS and TICS evidence two diffusive subpopulations of single GlyR pentamers. **A** Representative confocal microscopy image of the first frame from an image series of a HEK293 cell expressing GlyR-α3L-eGFP. Frame-based intensity thresholding was used to remove GlyR clusters and the extracellular region from the analysis. Scale bar 10 µm. **B** Photon count values fluctuating along the yellow arrow in (**A**). **C** 3D autocorrelation with the gray outlining showing the average (ξ, 0) and (0, ψ) autocorrelation function. D) Average (ξ, 0) and (0, ψ) autocorrelation function and fit. Top graph displays the weighted residuals for the fit in the bottom graph. **E** Average diffusion constant and standard deviation obtained via RICS for GlyR-α3L-eGFP and GlyR-α3K-eGFP. **F** Representative TIRF microscopy image of the first frame from an image series of a HEK293 cell expressing GlyR-α3L-eGFP. Frame-based intensity thresholding was applied to remove GlyR clusters (indicated in red) and the extracellular region (indicated in light gray). Scale bar 10 µm. **G** Camera count values fluctuating over time, measured at the position marked by the yellow cross in (**F**). **H** Average temporal autocorrelation function and fit. Top graph displays the weighted residuals for the fit in the bottom graph. **I** The average diffusion constant and standard deviation obtained via TICS for single GlyR-α3L-eGFP and GlyR-α3K-eGFP. Here, a dynamic mask was used, calculated per frame, to omit both mobile and immobile GlyR clusters from the analysis. ***$p < 0.001$ from a non-paired *t*-test. **J** The average diffusion constant and standard deviation obtained via TICS for GlyR-α3L-eGFP when co-expressed with GlyR-α3K-mCh or GlyR-α3L-mCh compared to co-expression of GlyR-α3K-eGFP with GlyR-α3K-mCh. Image masking was based on the average intensity of the time series, so only static clusters were removed. Error bars on the bar graphs represent the standard deviation from $n = 9$–22 different cell measurements (Tables S1–2). ***p value < 0.005 from a one-way ANOVA and Tukey's multiple comparisons test

a significantly slower diffusion of the L variant was always observed. In other words, when looking at diffusion of single pentamers of GlyR-α3 on the slow TICS timescale, the L variant exhibits a slower mobility than the K variant.

Finally, we wanted to investigate whether co-expression of K would affect the mobility of L at the level of pentamers. Practically, we co-expressed GlyR-α3L-eGFP and the red mCherry FP-tagged version of the short GlyR isoform (GlyR-α3K-mCh) and performed single-color TICS on the acquired eGFP channel image series. Interestingly, we observed an increased diffusion constant for GlyR-α3L-eGFP in the presence of GlyR-α3K-mCh (Fig. 2J, Table S2, $D = 0.061 \pm 0.01$ µm^2/s; the value is slightly different than in Fig. 2I because of the different mask used) as compared to cells co-expressing GlyR-α3L-eGFP and GlyR-α3L-mCh (Fig. 2J, Table S2, $D = 0.044 \pm 0.01$ µm^2/s) or as compared to GlyR-α3L-eGFP alone (Fig. S4D, Table S2, $D = 0.047 \pm 0.01$ µm^2/s). As expected, co-expression of GlyR-α3K-eGFP and GlyR-α3K-mCh (Table S2, $D = 0.068 \pm 0.01$ µm^2/s) did not affect the mobility of the former as compared to GlyR-α3K-eGFP alone (Table S2, $D = 0.074 \pm 0.01$ µm^2/s). These results are strongly indicative of a direct K-L interaction at the level of single pentamers, which we have further investigated using dual-color imaging as described below.

Co-localization and co-diffusion prove GlyR-α3L/K heteropentamerization

To investigate whether GlyR heteropentamerization could be the cause of the increased mobility observed for GlyR-α3L-eGFP when co-expressed with GlyR-α3K-mCherry in the membrane of HEK293 cells, we recorded dual-color images via alternating-excitation TIRF microscopy (Fig. 3A).

To quantify the similarity of the two images and hence the colocalization of the two splice variants in the membrane, we calculated the Pearson's correlation coefficient ρ (Eq. 8). The ρ describes the degree of correlation between green and red channel pixel intensities of a dual-color image [47, 48]. The values of ρ can range from 1 to −1, with 1 a perfect correlation, 0 when there is no correlation and −1 for when there is an inverse relationship (exclusion) between the images. The pixels included in the analysis were confined to the region of the cell membrane since the extracellular

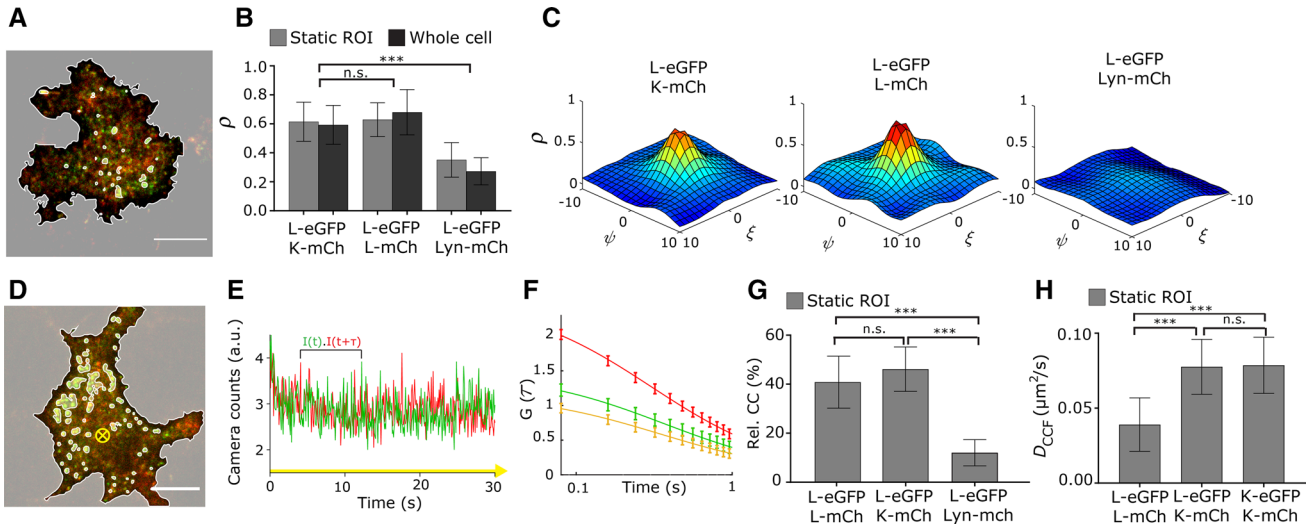

Fig. 3 Co-localization and co-diffusion of GlyR-α3 isoforms in HEK293 cells at single-molecule expression confirms the presence of GlyR-α3L/K heteropentamers. **A** Representative dual-color TIRF image of a HEK293 cell co-expressing GlyR-α3L-eGFP (green) and GlyR-α3K-mCherry (red). Using intensity thresholding over the average of the 5 first frames the cell membrane was selected and bright regions containing GlyR clusters were omitted. Scale bar 10 μm. **B** Pearson's correlation coefficient of cells expressing GlyR-α3L-eGFP and GlyR-α3K-mCherry and cells co-expressing GlyR-α3L-eGFP and GlyR-α3L-mCherry plasmids. Both experimental groups have significantly higher co-localization compared to the negative control with GlyR-α3L-eGFP and Lyn-mCherry. Lyn is a monomeric membrane protein that does not interact with GlyR. The ρ values are shown for cells including (gray) and excluding (dark gray) GlyR clusters. **C** Spatial ρ from representative cells expressing GlyR-α3L-eGFP and GlyR-α3K-mCherry (left), GlyR-α3L-eGFP and GlyR-α3L-mCherry (middle) or GlyR-α3L-eGFP and Lyn-mCherry (right). **D** Representative dual-color TIRF image of a HEK293 cell co-expressing GlyR-α3L-eGFP (green) and GlyR-α3K-mCherry (red). Intensity thresholding was applied over the average of the 400 frames (static ROI) to remove GlyR clusters and the extracellular region. Scale bar 10 μm. **E** Dual-color fluorescence trace for one selected pixel over time (yellow arrow orthogonal to the image in (**D**). **F** Mean temporal autocorrelation (green and red) and cross-correlation (yellow) of all included pixels after intensity thresholding. Error bars are the 95% confidence intervals. **G** The relative cross-correlation (Eq. 12) for cells expressing GlyR-α3L-eGFP and GlyR-α3K-mCherry, GlyR-α3L-eGFP and GlyR-α3L-mCherry plasmids, and the negative control with GlyR-α3L-eGFP and Lyn-mCherry. **H** Average diffusion constant and standard deviation obtained via TICCS for cells co-expressing GlyR-α3L-eGFP and GlyR-α3K-mCh or GlyR-α3L-mCh, or for cells co-expressing GlyR-α3K-eGFP and GlyR-α3K-mCh. Error bars represent the standard deviation from $n = 5$–22 measurements (see Table S2–3 for n). ***p-value < 0.005 from a one-way ANOVA and Tukey's multiple comparisons test.

region holds pixels with both low green and red intensity values which falsely increases the ρ value [49]. In addition, when cells contained regions with clustering GlyRs, these regions were also omitted by static ROI intensity thresholding to ensure Pearson's analysis was performed only on the heteropentamer fraction. This revealed a positive Pearson's correlation coefficient calculated for images of cells co-expressing GlyR-α3L and GlyR-α3K, similar to the one calculated for cells co-expressing GlyR-α3L labeled with eGFP and mCherry (Fig. 3B), and significantly higher than for the negative control cells co-expressing GlyR-α3L-eGFP and the monomeric membrane protein Lyn-mCherry that does not interact with GlyR. To confirm that the Pearson's coefficient was indeed determined mainly by the fluorescent receptors, and less by cellular background, ρ was calculated as a function of the pixel shift between the images in the x and y direction (Fig. 3C). For cells expressing GlyR-α3L and GlyR-α3K a clear positive peak was seen, indicative of real co-localization. For cells expressing non-interacting GlyR-α3L-eGFP and Lyn-mCherry, this peak was generally absent or very small and wide (Fig. 3C, right), indicative of non-specific co-localization.

A large Pearson's correlation coefficient indicates that proteins colocalize on a length scale smaller than or equal to the lateral resolution of the microscope. However, to more directly investigate the hetero-oligomerization of the slowly diffusing GlyR-α3 population we used dual-color cross-correlation TICS (TICCS) in HEK293 cells co-expressing GlyR-α3L-eGFP and GlyR-α3K-mCherry [32, 43]. For TICCS, image acquisition of the bottom membrane was performed using dual-color fast alternating TIRF-based excitation microscopy (Fig. 3D). For each pixel position in the image series, the fluorescence time traces (Fig. 3E) were temporally auto- and cross-correlated (Fig. 3F, Eq. 10). While the temporal autocorrelation and cross-correlation functions on their own allow determining molecular parameters such as mobility (Eq. 11), the relative cross-correlation additionally is a proof for their co-diffusion, and even a measure for the interaction affinity between them [50]. For cells co-expressing GlyR-α3L-eGFP and GlyR-α3K-mCherry we measured

a high relative cross-correlation (Fig. 3G, Eq. 12) that was similar to cells co-expressing GlyR-α3L-eGFP and GlyR-α3L-mCherry. This is a result from a similar high interaction affinity. Note that even for constantly interacting or even covalently linked molecules the maximum interaction value is typically around 50–60% (it never reaches the theoretical 100%) since it is limited due to factors such as incomplete fluorescent protein maturation or the partial overlap between green and red microscope detection volumes [51]. As a negative control, we analyzed cells containing GlyR-α3L-eGFP and Lyn-mCherry (Fig. 3G). We observed a very low cross-correlation amplitude (Fig. S4E) and significantly lower relative cross-correlation.

In contrast to single-color fluctuation experiments, dual-color TICCS offers the additional possibility to focus specifically on the diffusion properties of the heteropentameric complexes containing both eGFP and mCherry fluorophores. In line with the single-color experiments, these data also show that GlyR-α3L/K complexes exhibit higher diffusion constants compared to GlyR-α3L-eGFP/mCherry homopentamers (Fig. 3H, Table S2). Together, the Pearson's correlation and dual color TICCS experiments prove that GlyR-α3L and GlyR-α3K are localizing and diffusing as a complex. As the masked analyses we perform allow focusing on GlyR pentamers, this must mean the GlyR-α3K and GlyR-α3L splice variants can heteropentamerize. Moreover, heteropentamer diffusion resembles that of the short-loop splice variant K. We next wondered whether these heteropentamers existed in a defined heterostoichiometry or not.

The stoichiometry of GlyR heteropentamers depends on the relative subtype expression

To provide further insights into the stoichiometry of heteropentamers we performed two types of experiments: single-molecule step-wise photobleaching and molecular brightness analysis. For the first experiment, we performed continuous TIRFM single-molecule imaging of the eGFP labels in fixed cells co-expressing GlyR-α3L-eGFP and GlyR-α3K-mCherry and analyzed the resulting single-molecule traces with a step-finding algorithm to count the number of fluorescing eGFPs in a single complex (Fig. 4A). As the co-localization and fluctuation experiments showed that under such experimental conditions, these complexes are most likely heteropentamers containing both eGFP and mCherry fluorophores, it is expected that compared to samples containing GlyR-α3L-eGFP homopentamers (Fig. 1D), the number of eGFP moieties per complex should be lower. Indeed, the experimental data revealed a distribution with, on average, less eGFP subunits per spot compared to GlyR-α3L-eGFP homopentamers (Fig. 4B; Kolmogorov–Smirnov test $p < 0.01$).

We fitted the resulting step frequency distribution using two binomials, one representing the heteropentamer (up to 4 GlyR-α3L-eGFP subunits) and the other the homopentamer fraction (Eq. 2, Fig. 4C). The maturation probability (p_m) and probability of overlapping spots (1-A) was fixed to 47% and 12%, respectively, based on the experiments on homopentamers (Fig. 1D), while the relative fraction of heteropentamers was fitted. The goodness-of-fit obtained via the χ^2-test (Supplementary Table S4) was best for a 3rd order binomial and a heteropentameric fraction of 36% (goodness-of-fit p value from a χ^2 test = 0.725, with 1 being a perfect fit). However, as relatively good fits were obtained as well with a 2nd (p value = 0.332) or 4th (p value = 0.672) order binomial for a heteropentameric fraction of 23% and 67% respectively, these analyses are compatible with a scenario where heteropentamers contain on average 2–4 eGFP-containing subunits. It should be noted that fitting the binomial distribution to less than 10 data points is not very accurate, and having multiple good fits is to be expected.

For the molecular brightness analysis, we recorded a confocal image series of living cells expressing GlyR-α3L-eGFP alone, or together with GlyR-α3K-mCherry (Fig. 4D) and analyzed the molecular brightness in the eGFP detection channel via dynamic-ROI based RICS (Eq. 7). As expected, this revealed a significantly lower molecular brightness for L/K heteropentamers as compared to L homopentamers (Fig. 4E, Table S5). Interestingly, the molecular brightness calculated in the eGFP channel scaled with the signal (count rate) ratio of GlyR-α3K-mCh compared to GlyR-α3L-eGFP (Fig. 4F), and a few cells even exhibited a similar molecular brightness as observed for the monomeric control Lyn-eGFP, meaning the presence of heteropentameric GlyRs with only a single L-eGFP subunit.

Taken together, these experiments suggest the stoichiometry of GlyR-α3 heteropentamers is not fixed but variable, and depends on the relative expression of the L and K subtypes.

An intermediate electrophysiological signature for heteropentamers

At this stage, we revealed the existence of K/L heteropentamers and investigated their molecular organisation. Lastly, we wanted to investigate possible functional differences between heteropentamers and homopentamers. Indeed, this might help to understand the consequences of an aberrant L/K ratio as observed in TLE. Practically, we used cell-attached single-channel electrophysiology as opposed to whole-cell measurements to avoid averaging out activities of different co-existing species. Moreover, to verify the GlyR expression levels and ensure patch clamp measurements were performed under identical conditions

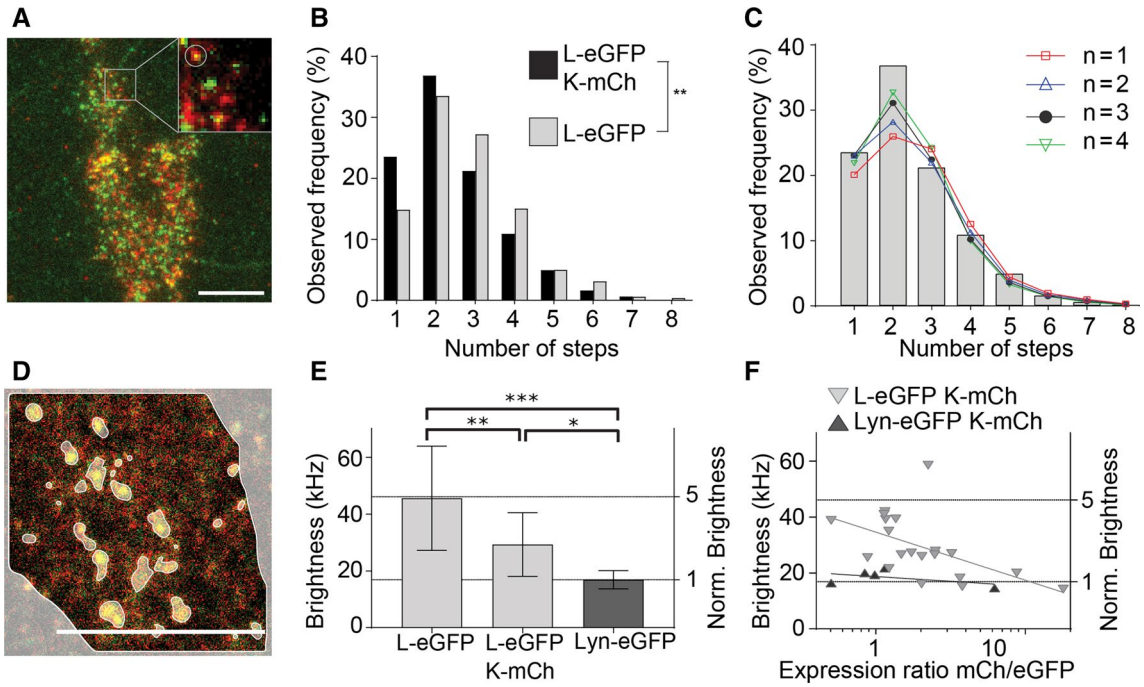

Fig. 4 Automated subunit analysis and molecular brightness analysis shows the effect of relative expression on the GlyR stoichiometry. **A** Representative images of HEK293 cells expressing GlyR-α3L-eGFP (green) and GlyR-α3K-mCherry (red). Scale bar 10 µm. **B** Step distribution histogram of GlyR-α3L-eGFP in the presence (light gray, 301 spots) and absence (black, 477 spots) of GlyR-α3K-mCherry. In the presence of GlyR-α3K-mCherry there is a significant shift towards a lower number of GlyR-α3L-eGFP subunits. $^{**}p$ value < 0.01 obtained with Kolmogorov–Smirnov test. **C** Fitted binomial distribution functions with a sum of a 5th order binomial and nth order ($n = 1$–4) binomial. See Table S4 for heteromeric fraction and p-value for the fit (χ^2-test). **D** Representative confocal microscopy image of the first frame from an image series of a HEK293 cell expressing GlyR-α3L-eGFP and GlyR-α3K-mCherry. Scale bar 10 µm. **E** Molecular brightness comparison of the membrane-bound monomeric protein Lyn-eGFP to GlyR-α3L-eGFP in either the presence or absence of GlyR-α3K-mCherry. Error bars represent the standard deviation from $n = 5$–20 measurements (see Table S5 for n). p value $<$ *0.05, **0.01, ***0.005 from a one-way ANOVA and Tukey's multiple comparisons test. **F** Molecular brightness of GlyR-α3L-eGFP (light gray) and monomeric Lyn-eGFP (dark gray) in the presence of variable amount of GlyR-α3K-mCherry. The semilog line fit shows a decrease in brightness for GlyR-α3L-eGFP upon increasing ratio of GlyR-α3K-mCherry to GlyR-α3L-eGFP

as the fluorescence experiments, the patch clamp setup was mounted directly onto the single-molecule fluorescence microscope used for the stepwise photobleaching and TICS/TICCS experiments (Fig. S2). Cells were transfected with either GlyR-α3L-eGFP or GlyR-α3K-mCherry, or with both. Importantly, the transfection conditions were similar to those used in the TICCS measurements, where we showed a high prevalence of heteropentamers for cells transfected with both plasmids. Via qualitative widefield fluorescence microscopy we selected lowly expressing cells with similar expression levels of the eGFP- and mCherry-tagged isoforms (Fig. 5A). We then performed cell-attached single-channel electrophysiology to determine the currents (Fig. 5B–D). For the different transfection conditions, currents on the ~ 1–10 pA range were observed, with the mean current for the K variant being significantly higher than that for the L variant. Cells expressing both variants seemed to exhibit intermediate current levels.

Discussion

The glycine receptor is a ligand-gated chloride channel that plays a crucial role in the general physiology of the CNS. Its α3 isoform, in particular, is involved in epilepsy and chronic pain [5, 9, 26]. Two splice variants of α3 exist (Fig. 1A). As homopentamers, the splice variants differ in subneuronal distribution, electrical conductance and desensitization, clustering tendency, interactions with subcellular components and diffusion properties [3, 5, 8, 20–22], yet it is not known whether L and K variants can heteropentamerize. Indeed, such a process may lead to new or intermediate properties, or properties biased more towards one variant or the other. In an attempt to provide a more detailed fundamental cell-biological understanding of the working of GlyR-α3, we thus investigated the hypothesis that the different splice variants of GlyR-α3 can assemble into functional heteropentamers. To prove this hypothesis via advanced fluorescence imaging we first had to set up a new quantitative image analysis methodology for studying single pentamers in a complex

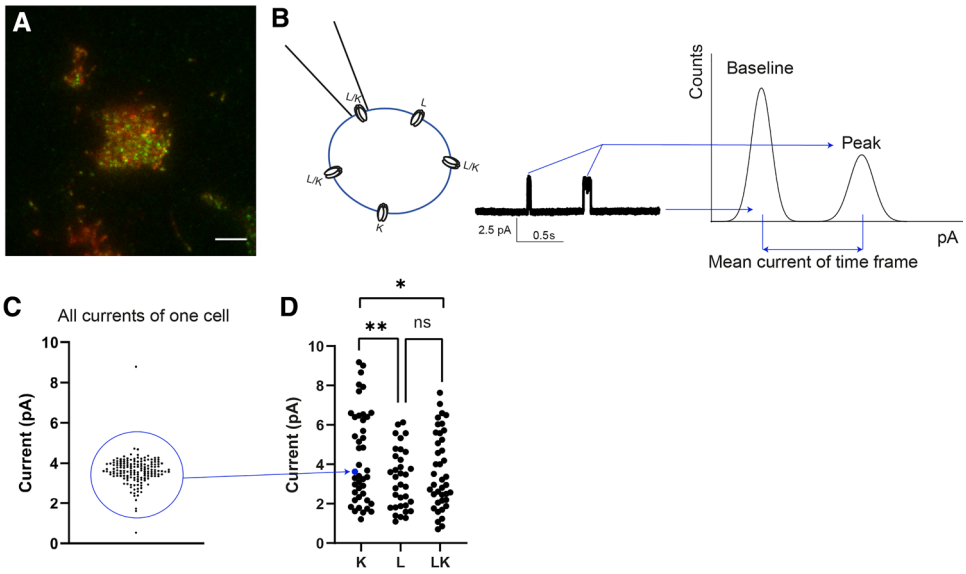

Fig. 5 Single-channel measurements show activated α3K yields higher currents. **A** Transfected cells are identified by eGFP or mCherry fluorescence. Scale bar is 5 µm. **B** Left: Illustration of cell-attached single-channel electrophysiology: single receptors are exposed to glycine (30–80 µM) present in the patch pipette. Middle: example of a current time trace during which similar peak currents are seen. Right: A histogram of all measured currents is fit with a double Gaussian, yielding a best fit value for the mean baseline current and the mean peak current. Subtracting the mean baseline current from the mean peak current yields the mean current for the time frame. **C** Example of all mean currents obtained from the window-based analysis illustrated in panel (**B**) for one cell. The number of current samples per cell varied from a few to over 300. Similar currents are grouped together to allow an unbiased comparison of different cells and transfection conditions. Some cells yielded more than one group of currents. **D** All groups of currents for cells transfected with α3K (25 cells), α3L (23 cells) and α3K + α3L (27 cells) are shown. A one-way ANOVA with Tukey's multiple comparisons test showed significantly higher currents for α3K as compared to α3L or α3L + α3K. *p* value < *0.05, **0.01, ns = not significant

sample, cell membranes containing both single pentamers and clusters of the same protein. Then, using this methodology we revisited prior work on the diffusion properties of GlyR-α3 splice variants in HEK293 cells to unequivocally prove whether RNA splicing determines the membrane mobility of the protein. Only hereafter could we embark on proving the existence of GlyR-α3L/K heteropentamers, and on quantifying their molecular and functional properties.

Tools for studying defined molecular species in the case of oligomerization/clustering

A first methodological aim was to set up the necessary experimental tools to quantify single GlyR-α3 pentamer properties in cells. This is particularly challenging because of the tendency of GlyR-α3 to form subcellular clusters [5, 22, 23, 52, 53] that would overshadow the analysis. In previous research done by Notelaers et al., GlyR-α3 properties were investigated using fluctuation spectroscopy, single-molecule and super-resolution fluorescence methods, yet it was not explicitly investigated which observed species were representative of single pentamers or clusters [20–22]. Indeed, although image correlation spectroscopy (ICS) methods are quite robust in quantifying concentrations, diffusion and stoichiometry for monodisperse samples [54], they perform particularly badly in the case of polydisperse ones containing clusters, aggregates or multimeric species [55–57]. Here, we exploited the molecular fluorescence brightness of fluorescent protein labeled GlyR splice variants to validate that our methodology does specifically allow studying single pentamer properties. On the one hand, we performed subunit counting via stepwise photobleaching [33, 34] experiments in low-expressing cells in which fluorescent homomeric GlyR-α3L-eGFP was present as clearly discernable fluorescent spots (Fig. 1C–D). This way we found that the number of fluorescence bleaching steps per spot was similar to the previously studied GlyR-α1 under non-clustering conditions in HEK293 cells [33, 39]. On the other hand, we used a more recent extension of classical ICS called arbitrary-region ICS (ARICS) [55], where image series are segmented based on the local pixel fluorescence intensity, to specifically quantify the average molecular fluorescence brightness for single GlyR pentamer complexes diffusing in the live cell membrane (Fig. 1E–H; Video S1–2). With this analysis, we could show that results for (the more clustering-prone) homomeric GlyR-α3L-eGFP expressing cells were in line with non-clustering stoichiometric control proteins. This finally proved that our cellular expression system, HEK293 cells expressing fluorescent protein labeled GlyR splice variants from a crippled CMV promotor, and

single-molecule photobleaching and segmented ICS analyses, are adequate for studying single pentamer properties, even when a non-negligible clustering subpopulation is present. Apart from the investigations performed in the rest of our paper, the methodological toolbox presented here can be applied for examining protein interactions, oligomerization, mobility and stoichiometry of other oligomeric receptors or multimeric proteins. For example, given the sequence similarity and distribution of different GlyR isoforms in the CNS, it could be investigated whether different GlyR isoforms can also heteropentamerize, and if so, what the functional consequences would be. Also, relative to the original methodological publication on segmented ICS [55] (detailed protocol in [58]), we did extend our in-house developed software for robust segmented single- and dual-color raster and temporal ICS analysis. This software can be downloaded free-of-charge (see "Materials and methods"), is fully documented (https://pam.readthedocs.io/en/latest/mia.html), can be operated via a convenient graphical user interface from Microsoft and Apple operating systems, accepts a variety of images/videos, and can export figures and videos directly in publication-format.

Specific subcellular interactions of single GlyR-α3L pentamers decrease their membrane mobility

Physiologically, GlyR-α3 is present in cells both as clustered and single pentamers. While α3K is more randomly distributed over the cell membrane, the situation for α3L is balanced somewhat more in favor of clusters [5, 22]. The α3L interacts with submembranous components specifically enriched at the presynapse, where it can promote (at glutamatergic nerve termini) neurotransmitter release [8]. Functionally, clustering of α3L thus seems to be an efficient way to promote this local enrichment. Notelaers et al. previously reported that overall, the subcellular mobility of α3L was lower than of α3K [20, 21]. For systems undergoing Brownian diffusion, the mobility (more specifically, the translational diffusion constant) of a freely diffusing entity scales inversely with its size (Einstein-Smoluchovski relation). For membrane proteins in particular, mobility scales with the radius of the transmembrane region [59, 60]. For the specific case of GlyR-α3L, receptor clustering would increase the size of the diffusing complex, and this would reduce mobility. Likewise, however, strong interactions of GlyR-α3 with large or immobile sub-membranous components would also likely reduce its overall mobility.

As a follow-up of the work of Notelaers et al., we investigated whether a difference in single-pentamer mobility between the L and K variants can also be detected using our experimental setup. To this extent, we performed both confocal and TIRF-based microscopy and ICS analysis of GlyR-α3 expressing HEK293 cells to study the diffusion properties of the two splice variants. We segmented the images before ICS analysis to exclude those pixel regions containing GlyR clusters. Via confocal raster ICS (RICS) analysis we observed a fast freely diffusing component for both isoforms with similar diffusion constants ($D_{\alpha3L} = 0.26 \pm 0.11$ μm^2/s and $D_{\alpha3K} = 0.29 \pm 0.08$ μm^2/s) (Fig. 2A–E, Table S1). The existence of this freely diffusing component, that has been described before [21], suggests that at least a fraction of the GlyR-α3 population does not interact with immobile cellular components, or that the mere limited affinity for the latter defines the presence of a significant unbound component. The presence of functional GlyRs with relatively high mobility is, however, not surprising. It could allow for a faster reconstitution of non-desensitized GlyR receptor pools, as has been shown previously for the AMPA receptor, another ligand-gated ion channel [61]. When we studied the diffusion of single GlyR-α3 pentamers using TIRF-based temporal ICS (TICS), we observed a second, much less mobile species for both splice variants, which, interestingly, was even less mobile for α3L as compared to α3K ($D_{\alpha3L} = 0.057 \pm 0.014$ μm^2/s and $D_{\alpha3K} = 0.089 \pm 0.023$ μm^2/s) (Fig. 2F–I, Table S1–S2). This observation, in term, strongly suggests that the 15-residue-longer loop of GlyR-α3L relative to GlyR-α3K does indeed stabilize interactions with cellular interaction partners such as proteins or lipids, independent of GlyR clustering [8]. For primary neuron hippocampal cells, vesicular transport protein SEC8 targets the GlyR-α3L to the presynapse, and in vivo, GlyR-α3L was indeed detected at presynaptic terminals of glutamatergic and GABAergic neurons [8]. An interesting follow-up study would be to use site-directed mutagenesis of the insert region to more closely study sequence motifs of GlyR-α3L binding partners that control axonal receptor trafficking and localization. Conversely, GlyR-α3K is mainly distributed somatodendritically, but is also expected to be present in axonal and presynaptic compartments as this splice variant lacks a subcellular targeting signal and hence diffuses throughout the neuronal plasma membrane. This notion is furthermore supported by a recent study showing that there is no GlyR-β protein expression in hippocampal neurons [62], which could target the GlyR-α/β heteropentamers to postsynaptic gephyrin-positive scaffolds [19, 63].

GlyR-α3L and GlyR-α3K splice variants form heteropentamers of variable stoichiometry

Co-clusters of GlyR-α3 splice variants have already been reported [22]. The single-color TICS experiments we performed in the present study, however, provided a first hint towards a direct interaction between α3L and α3K splice variants in the form of heteropentamers, since co-expression of α3K increased the mobility

of single α3L pentamers ($D_{\alpha3L} = 0.047 \pm 0.012$ μm^2/s and $D_{\alpha3L+K} = 0.061 \pm 0.011$ μm^2/s) (Table S2). Hetero-oligomers of different isoforms of GlyR-α/β [64] and of other ion channels such as the NMDA receptors have been described before, and also the biogenesis of GlyR-α3 would be compatible with it [65]. For GlyR-α3 they are of specific interest because of the differential subcellular localization of splice variants [8] and because of their different electrophysiological desensitization signatures [3].

To provide a more conclusive answer, we first demonstrated co-localization between GlyR-α3L and GlyR-α3K upon co-expression in HEK293 cells using a spatial version of Pearson's colocalization analysis that is more robust against coincidental pixel co-localization (Fig. 3A–C, Fig. S4H, Table S3) [47, 66]. Subsequently, we used dual color temporal ICS (TICCS) to unequivocally demonstrate, for the first time, heteropentamerization of GlyR-α3L and GlyR-α3K (Fig. 3D–G, Table S2). Finally, we employed direct subunit counting via stepwise photobleaching to quantify that the average stoichiometry of heteropentamers is 2–4 α3L-eGFP-containing subunits (Fig. 4A–C, Table S4). A non-negligible homomeric fraction was also present in all datasets, which furthermore supports the absence of a defined heterostoichiometry. Direct subunit counting via stepwise photobleaching was previously used to show that α1 and β isoforms, genetically labeled with fluorescent proteins, heteropentamerize in a $\alpha_3\beta_2$ stoichiometry [64]. Finally, we carried out molecular brightness analysis to reveal that the heterostoichiometry is indeed variable and depends on the expression ratio of both splice variants (Fig. 4D–F, Table S5). Putting all stoichiometry data together we did not provide any evidence for a highly specific α3L/K stoichiometry.

GlyR-α3L/K heteropentamers have GlyR-α3K-like mobility and intermediate conductance characteristics

The presence of heteropentamers can have several implications for GlyR-α3 function. In this paper, we investigated the subcellular mobility and electrophysiological signature of heteropentamers. Single-color TICS provides a readout of mobility, and evidenced that co-expression of α3K increased the mobility of α3L (Fig. 2J, Table S2). Of course, in the case of a subcellular mixture of homo- and heteropentamers, such single-color measurements only provide an average view, which is why we next performed a mobility analysis of only those species containing both α3K and α3L via image cross-correlation analysis via dual-color temporal ICS (TICCS) (Fig. 3H, Table S2). From these experiments it became apparent that the diffusion signature of the K isoform is dominant for the mobility of the heteropentamers. This additionally suggests that the subcellular interactions of α3L that render its mobility slow are multivalent rather than monovalent. As many as 5 subunits of α3L thus seem to be needed to result in its homomeric mobility signature. This might mean that the affinity of subcellular interactions of α3L is rather low, and that an avidity effect leads to the observed reduced mobility of homomers. Finally, combined cell-attached electrophysiology and fluorescence microscopy allowed us to investigate the single channel currents of GlyR-α3 in cells expressing GlyR-α3L-eGFP, GlyR-α3K-mCherry or both. Contrary to what is known from literature [25, 26, 28, 29], our data quite clearly evidenced that α3K-only expressing cells exhibited larger currents than α3L-only expressing cells. Cells expressing both variants did not exhibit currents that were significantly different from those expressing only the L variant, yet a trend towards current values intermediate to K- or L-only cells was present. In essence, this variety of conductance levels between those of GlyR-α3L and GlyR-α3K would be in line with our stepwise-photobleaching analyses that suggested an indeterminate L-to-K heteropentamer stoichiometry. We must state that these currents, and the overall spread thereof, can be affected by differences in intracellular Cl^- concentrations. To investigate this, we performed outside-out patch electrophysiology (Fig. S6). These experiments evidenced on the one hand that the actual conductances for the different cell types we analyzed are in line with literature values, and on the other hand a higher conductance of the K relative to the L-variant expressing cells, corroborating the cell-attached measurements (Fig. 5).

As GlyR-α3L adopts the mobility signature of GlyR-α3K in heteropentamers, in regions of the brain where co-expression of GlyR-α3L and GlyR-α3K occurs, this could mean that heteropentamerization influences GlyR renewal in the plasma membrane, and as a result GlyR functionality. Consequently, this further stresses the importance of well-regulated alternative splicing for GlyR-α3 signaling. As in healthy people there is an increased presence of GlyR-α3L compared to GlyR-α3K, a small increase in alternative splicing would influence even more GlyR-α3L pentamers due to heteropentamerization. Due to heteropentamerization a higher fraction of GlyR-α3L containing pentamers will have a higher mobility, which could enable faster reconstitution of the non-desensitized GlyR receptor pool [61]. The results from electrophysiology in particular also point to the possibility that the neuronal output can be modulated by GlyR-α3 heteropentamers, particularly in conditions such as TLE where increased RNA editing and resulting gain-of-function receptors modulate the homeostatic regulation of the neuronal output [8, 14]. Importantly, subcellular trafficking and localization (pre- or postsynaptic, or, e.g. in the distal and basolateral membrane compartments of epithelial cells) must be logically and interpretively distinguished from terms that describe single channel signatures of mobility

and electrophysiology (currents). Indeed, a single receptor pentamer with specific mobility and conductance states can lead to very different outcomes depending on its subcellular localization. For example, due to its very small surface, the electrical capacity (C) of a presynapse is much lower compared to the somatodendritic compartment, and hence, one single channel conductance of chloride ions (Q) through the presynaptic plasma membrane will have a much greater impact on membrane potential (U) compared to the same conductance in the somatodendritic compartment ($\Delta U = Q/C$).

Conclusion

In this work, we investigated the long (L) and short (K) intracellular loop splice variants of the GlyR-α3 isoform, that is related to chronic pain and temporal lobe epilepsy. We unambiguously showed that these splice variants co-assemble into electrophysiologically active heteropentamers in live HEK293 cells. To do this, we had to set up and validate a combination of advanced single-molecule fluorescence, fluorescence fluctuation correlation and patch clamp methods, as the GlyR-α3 tends to cluster inside cell membrane, and this clustering is extraordinarily challenging for quantitative investigations. First and foremost, this work constitutes a methodological framework that can be used for investigating other types of complex hetero-oligomerizing molecular systems in a cell-biological context. Biologically, it turned out that, while the GlyR-α3L was well known to determine the subcellular localization of GlyR-α3 channels, GlyR-α3K is leading in the regulation of the in-membrane mobility of GlyR-α3 and heteropentamers adopted conductances in between those of the respective homomers. Future research could be aimed at studying GlyR heteropentamer clustering, localisation and activity somatodendritically or presynaptically in primary neuron cells or even in vivo in mouse models. Likewise, measuring channel open times would prove that heteropentamerization is important for fine-tuning of neuronal activity, which would, in turn, provide insights into the desensitization behaviour of heteropentamers.

Materials and methods

DNA plasmids

Plasmids encoding mouse (99% identical to human, i.e., 4/464 residues difference) GlyR-α3L or α3K containing an N-terminal eGFP or mCherry were already described [67] or obtained accordingly using standard molecular cloning technology by replacing mCherry with eGFP. N-terminal eGFP insert was amplified with PCR (5'-CGGTCTCCGGAATGGTGAGCAAGGGC-3' and 5'-GGCCTCCGGACTTGTACAGCTCGTCCATGC-3'), the GlyR-α3L/K plasmids and the amplified eGFP insert were digested with BspE1. The vector plasmids were treated with calf intestine phosphatase before the ligation was performed. The enhancer region of the cytomegalovirus promotor in the GlyR-α3-coding plasmids was shortened similar as in [37] to reduce expression levels by mutagenesis. We did this by amplification of the GlyR-FP plasmids using PCR with primers 5'-ATATGGTACCTGGGAGGTCTATATAAGCAGAG-3' and 5'-ATAAGGTACCCCAGGCGGGCCATTTACCGTA-3' followed by digestion with KpnI (ThermoFisher Scientific, Merelbeke, Belgium) and ligation using instant sticky-end ligase Master mix (NEB, Bioké Leiden, Nederland). Plasmids used as a negative control (Lyn-FP) were first used in [68] as a negative control for membrane receptor dimerization and encode the tyrosine-protein kinase Lyn coupled to a fluorescent protein eGFP or mCherry. Plasmids expressing eGFP or an oligomeric chain of 3 or 5 eGFPs (eGFP, $eGFP_3$ and $eGFP_5$) previously used in [69] were used as an stoichiometric reference.

Cell culture and transfection

Human embryonic kidney 293 cells (HEK293 cells, provided by Dr. R. Koninckx, Jessa Hospital, Hasselt, Belgium) were cultured up to a maximum passage number of 20, at 37 °C and under a humidified 5% CO_2 atmosphere in complete DMEM medium (D6429, Sigma-Aldrich, Overijse, Belgium) supplemented with 10% FCS (Sigma-Aldrich). At least 24 h before transfection, 150,000 cells were plated in complete medium in a 35-mm diameter #1.5 (170 µm glass thickness) glass bottom dish (MatTek, Bratislava, Slovak Republic). Cells were transfected via calcium phosphate-DNA co-precipitation [70]. The phosphate-DNA mix contained 86 µL HEPES-buffered saline (HBS) (280 mM NaCl, 10 mM KCl, 15 mM D-glucose, 1.5 mM $Na_2HPO_4.2H_2O$, 50 mM HEPES, pH 7.1) and 2000 ng total plasmid DNA per dish including the 50–1000 ng FP-tagged encoding plasmids supplemented with an empty plasmid vector (pCAG-FALSE, Addgene plasmid #89689) depending on the aimed fluorescence level [38]. To this mix 5.1 µl 2.5 M $CaCl_2$ was added, and after 10 min of incubation at room temperature (RT) the mix was added dropwise to the cells.

Immunostaining

The day after transfection HEK293 cells were fixed using a − 20 °C pre-chilled mixture (95/5) of methanol and glacial acetic acid for 10 min at − 20 °C. Following three wash steps with PBS, α-GlyR (mAb4a, 1:100, # 146 011, Synaptic Systems, Göttingen, Germany), α-GFP (1:100, #ab290, Abcam, Boston, MA, USA), and

α-RFP (1:200, #390004, Synaptic Systems, Göttingen, Germany) antibodies were incubated with cells in PBS-gelatin (0.1%) solution at room temperature for 60 min. Following three wash steps with PBS-gelatin secondary antibodies coupled to FITC, TRITC, or Cy5 were incubated for 45 min at room temperature. After three wash steps with PBS-gelatin and one wash step with PBS the stained coverslips were mounted on glass slides using DAPI-containing Vectashield solution (Vector Laboratories, Burlingame, California, USA) and sealed with nail polish. A Zeiss ELYRA PS.1 inverted microscope with a Plan-Apochromat 100x/1.46 oil DIC M27 objective lens and PCO Edge 4.2 sCMOS camera was used in total internal reflection fluorescence (TIRF) mode to selectively excite molecules near (< 200 nm) the bottom cell membrane. Images were recorded at room temperature using a 642 nm HR Diode laser and a LP655 emission filter for the Alexa Fluor 647 signal; a 561 nm HR DPSS laser and a BP570-650 + LP750 emission filter for the TRITC signal; a 488 nm HR Diode laser and a BP495-575 + LP750 emission filter for the FITC signal; a 405 nm HR Diode laser and a BP420-480 + LP750 emission filter for the DAPI signal. Images were collected at a resolution of 1280 × 1280 pixels^2 and a pixel size of 62.5 nm. The fixing and mounting procedure resulted in a similar refractive index of the sample and cover glass. As this negatively influenced the total internal reflection fluorescence (TIRF) imaging, the images do not only reveal membrane-localized GlyR, but are partially contaminated by cytosolic contributions. This cytosolic fraction could represent incompletely synthesized protein that could not be targeted by the antibody, while containing a functional fluorescent protein tag.

TIRF imaging for subunit counting and TICS

A Zeiss ELYRA PS.1 inverted microscope with a Plan-Apochromat 100x/1.46 oil DIC M27 objective lens and Andor iXon + 897 EMCCD camera operated at EM gain ~ 200 was used in total internal reflection fluorescence (TIRF) mode to selectively excite molecules near (< 200 nm) the bottom cell membrane. Images were recorded at room temperature using a multiband emission filter LBF 488/561 at a resolution of 256 × 256 pixels^2 and a pixel size of 150 nm. The 488 nm and 561 nm HR diode-pumped solid-state lasers were used. The reported laser powers were measured on the objective lens with immersion oil using a calibrated S170C microscope slide power sensor head (Thorlabs, Dortmund, Germany). Imaging was done using the ZEN software (Zeiss).

Subunit counting by photobleaching analysis

TIRF images were acquired as described above using cells transfected with 50 ng GlyR-α3L-eGFP and 0–500 ng GlyR-α3K-mCherry which were fixed 22 h post-transfection for 24 h at 4 °C using 3% (w/V) paraformaldehyde in phosphate buffered saline. Before acquiring the images for the photobleachinig analysis, in each cell mCherry was photobleached with the 561 nm laser (5% power, 2.5 mW) in order to eliminate Förster resonance energy transfer between eGFP and mCherry. Next, 2000 frames were acquired at 100 ms per frame using the 488 nm laser at high enough power to induce step-wise photobleaching (1.5% power, 660 µW). Data analysis was performed using the Progressive Idealization and Filtering (PIF) software kindly provided by Dr. Rikard Blunck [33]. Molecules were located by selecting of 5 × 5 pixels^2 spots with the signal-to-noise (δ *F/F*) setting at 20%. Next, intensity time traces were extracted from a 3 × 3 pixels^2 region in the center of each spot. Partially overlapping spots were excluded from analysis. Photobleaching steps were identified via a step-finding algorithm when steps had a minimum length of 3 frames, and steps were not allowed to vary more than 60% in amplitude compared to other steps in the time trace. In addition, a minimal step signal-to-noise value of 2 was required. Cells with more than 10% accepted traces were included in the step frequency histogram. The step distribution of cells expressing only GlyR-α3L-eGFP was analyzed using the sum of the following two binomial distributions:

$$B(x;n+2n,p_m) = A\frac{n!}{x!(n-x!)}{p_m}^x(1-p_m)^{n-x} + (1-A)\frac{2n!}{x!(2n-x!)}{p_m}^x(1-p_m)^{2n-x}, \quad (1)$$

where B is the likelihood of observing x bleaching steps, n is the number of fluorescent eGFP molecules present in a single GlyR complex ($n = 5$), p_m is the probality that the fluorophore is maturated and non-bleached at the start of the recording, A is the fraction of spots containing not more than one GlyR complex and *1-A* is the fraction of spots containing two GlyR complexes. This equation assumes the fraction of spots containing more than two pentamers is negligible. In general, the p_m-value reported in studies using subunit counting via stepwise photobleaching is typically on the low side (50–80%) [33, 34, 71] compared to other studies (~ 80%) [72, 73]. The broad range is appointed to variability between experimental groups such as the used cell line, fluorescent protein [74], temperature during maturation [33], cell fixation and fluorophore prebleaching [75].

To describe the step distribution of cells expressing both GlyR-α3L-eGFP and GlyR-α3K-mCherry and determine

the stoichiometry (het) of the heteropentamers, Eq. 1 was extended as follows:

$$B(x;n+2n+\text{het}+2\text{het},p_m) = H\left[B(x;n+2n,p_m)\right] + (1-H)\left[B(x;\text{het}+2\text{het},p_m)\right]. \quad (2)$$

Here H represents the fraction of homopentamers and $1\text{-}H$ represents the fraction of heteropentamers in the sample. Fitting this equation to the bleaching histograms of cells transfected with both, GlyR-α3L-eGFP and GlyR-α3K-mCherry, gives best fit values for H and het. Goodness-of-fit was determined using the chi-squared test. A good fit is indicated by a low χ^2 value with $p > 0.05$, the model does not fit the data if $p < 0.05$ [64]. The mCherry was not sufficiently bright or photostable for similar single-molecule step-wise photobleaching analysis.

Correlation analysis

Fluctuation imaging and co-localization analyses were performed in the software package PAM [76]. In all equations that follow, pre-processed intensity images $I_i(x,y,t)$ are converted into fluctuation images $\delta I_i(x,y,t)$ prior to correlation analysis by subtracting the mean image intensity $\langle I_i \rangle$:

$$\delta I_i(x,y,t) = I_i(x,y,t) - \langle I_i \rangle, \quad (3)$$

where i is the imaging channel, (x,y,t) denote the pixel coordinates and the angled brackets represent the average of all pixels included into the region-of-interest used for analysis.

Raster image correlation spectroscopy

We used an inverted Zeiss LSM880 laser scanning microscope with a Plan-Apochromat 63x/1.4 Oil DIC M27 oil objective and MBS488/594 beam splitter to image live cells transfected with 100 ng GlyR-α3L-eGFP, 100 ng GlyR-α3K-eGFP or 50 ng Lyn-eGFP alone and/or combined with 0–1000 ng GlyR-α3K-mCherry, between 22 and 28 h post-transfection. Since RICS is ideally suited for capturing fast dynamics [32, 41, 44], the cells were held at 37 °C. However, to allow comparisons of RICS and TICS data, we did carry out limited RICS experiments at RT too (Fig. S4F). This revealed that the species observed with RICS still exhibited faster diffusion than those observed with TICS when measured at RT, and thus indeed represents a different subpopulation. Images were collected using parameters appropriate for RICS [45], i.e. 256×256 pixels^2 with a 50 nm pixel size. Pixel dwell, line and image times were 8.19 µs, 4.92 ms and 1.26 s, respectively. The eGFP species were excited with a 488 nm argon-ion laser (0.3%, 1 µW) and mCherry species with a 594 nm HeNe laser (1%, 6 µW). Fluorescence was detected using a spectral detector (Zeiss Quasar) operated in photon counting mode in 23 spectral bins with ~9 nm bin width ranging from 490 to 695 nm. For quantitative analysis of eGFP-tagged molecules, bins 1–11 (490–589 nm) were summed for further analysis. Prior to autocorrelation analysis, we excluded contributions from slow processes such as cell and cell organelle movement using a moving average correction according to [42, 44, 77]:

$$I_{\text{RICS}}(x,y,f) = I(x,y,f) - \langle I(x,y,f)\rangle_{\Delta F} + \langle I\rangle_{\text{XYF}}, \quad (4)$$

in which $I(x,y,f)$ corresponds to each individual image, $\langle I(x,y,f)\rangle_{\Delta F}$ is the local mean image calculated over a short 3-frame interval from frame $f-\Delta F$ to frame $f+\Delta F$ with $\Delta F = 1$, and $\langle I\rangle_{XYF}$ is the mean intensity over all frames. Next, pixels outside the cell were removed by freehand-drawing based selection of the cell membrane, while GlyR clusters were removed using frame-based intensity thresholding. Specifically, both green and red images were first individually masked by intensity thresholding to remove (equalize to zero) pixels belonging to high-intensity clusters of fluorescence [55]. A pixel was excluded from further analysis when the spatial mean intensity of that pixel and a selection (~5×5) of surrounding pixels was at least three times higher than the mean intensity of all included pixels in the total moving-average-corrected (Eq. 4) image series. The final mask contained pixels that were included in each individual image's mask and was smoothed using a 3×3 median filter as described above for co-localization analysis. Subsequently, the autocorrelation function was calculated per image frame using the arbitrary region-of-interest RICS (ARICS) algorithm [55]:

$$G(\xi,\psi) = \frac{\langle \delta I_{\text{RICS}}(x,y)\cdot \delta I_{\text{RICS}}(x+\xi,y+\psi)\rangle}{\langle I_{\text{RICS}}\rangle^2}, \quad (5)$$

in which ξ and ψ are the spatial lags in pixels, the $\cdot$ is the correlation operator, the angled brackets represent the average of all included pixels within the mask and $\langle I_{\text{RICS}}\rangle$ is the average of all moving-average corrected pixels included into the region-of-interest used for analysis. To compare different datasets, we often plot only the $(\xi, 0)$ correlations (example in Fig. 1F) or $(\xi, 0)$ and $(0, \psi)$ correlations (example in Fig. 2D). Finally, the autocorrelation function was fitted with a one-component model assuming a two-dimensional Gaussian point spread function to obtain the apparent diffusion constant, D, and average number of molecules in the focus, N.

$$G(\xi,\psi) = \frac{\gamma}{N}\left(1+\frac{4D\left|\xi\tau_p+\psi\tau_l\right|}{\omega_r^2}\right)^{-1}\exp\left(-\frac{\delta r^2\left(\xi^2+\psi^2\right)}{\omega_r^2+4D\left|\xi\tau_p+\psi\tau_l\right|}\right). \quad (6)$$

Here γ is the shape factor for a 2D Gaussian and equals $2^{-3/2}$ [78], τ_p and τ_l are pixel and line dwell times, δ_r is the

pixel size and ω_r the lateral waist of the focus determined by calibration measurements (Fig. S5B). The RICS data were also used for calculating the molecular brightness of eGFP-containing diffusing molecules. Brightness (ε), expressed in kilophotons emitted per diffusing complex per second (i.e. kHz) at the center of the confocal spot, was calculated by dividing the mean intensity of the image series (F) by the number of molecules obtained via RICS autocorrelation analysis (N_{ACF1}) as follows:

$$\varepsilon = \frac{F}{N_{\mathrm{ACF1}}}. \tag{7}$$

Indeed, in image correlation spectroscopy applications where absolute photon counts are recorded and binned into the images, the pixel intensities and molecular brightnesses are commonly expressed in kHz, with 1 kHz being 1000 photons registered by the imaging system per second. For example, for a molecule imaged at 50-kHz brightness and 10-µs pixel dwell time, on average 1 photon is registered every two pixels. As stoichiometric references, cells were transfected with 5–10 ng eGFP, $eGFP_3$ or $eGFP_5$ encoding plasmids and investigated 22–28 h post-transfection as described above. When determining N, the moving average correction bias on the correlation amplitude was also corrected for as described before (Eq. 11 in [55]). Finally, stably focusing on the bottom membrane was achieved using a Zeiss Definite Focus.2 which acquired 60 frames at two different z-positions above the coverslip with an interval of 0.4 µm, alternating height each image frame, after which the time series at the z-position with highest average intensity was selected for analysis. We did also observe a clear effect of focus height above the coverslip on the molecular brightness, but not on the diffusion constant as shown in Fig. S4G, and as described before [44]. Finally, RICS was performed at low (µW) laser powers that avoid significant photobleaching, the latter of which would corrupt the resulting data. To obtain a proper signal-to-noise ratio of the resulting correlation data, and to avoid that the required total measurement time would be incompatible with the time scale of spontaneous cell movements, we therefore carried out RICS experiments at concentration levels which were appr. 20- to 100-fold higher than the single-step photobleaching experiments. However, these expression levels are still physiologically relevant: GlyRa3 has been shown to be present at > 1000 complexes per µm^2 in synaptic regions where it forms clusters, and as low as ~ 3 complexes per µm^2 in extrasynaptic regions where it is mostly present as single pentamers [22]. Combined, our model experiments in HEK293 cells recapitulate these two situations well: in our single-step photobleaching experiments around 1–2 receptors were present per µm^2 (estimated visually), and in the RICS experiments between ~ 20 and 200 receptors per µm^2 (calculated from N in Eq. 6).

Pearson's co-localization analysis

A 400-frame TIRF image series of live cells transfected with 100 ng GlyR-α3-eGFP and 150 ng GlyR-α3-mCherry or 50 ng Lyn-mCherry was acquired 22–28 h post transfection at 80 ms per frame using alternating 2-color excitation. The eGFP species were excited during 20 ms at 488 nm (0.75% power, ~ 330 µW), followed by 20 ms excitation of the mCherry species at 561 nm (1.5% power, ~ 750 µW). A modified image correlation calculation was used to calculate the Pearson's correlation coefficient ρ and to check the specificity of ρ [47, 66, 79, 80]. Image masking was performed as for RICS analysis. The ρ of the masked images was then calculated using the following equation:

$$\rho(\xi,\psi) = \frac{\langle \delta I_1(x,y) \cdot \delta I_2(x+\xi, y+\psi)\rangle}{\langle \sigma_1 \rangle \langle \sigma_2 \rangle}, \tag{8}$$

where σ_i is the average standard deviation of the fluorescence intensity of all pixels included into the region-of-interest used for analysis.

The $\rho(0,0)$ is the classical Pearson's coefficient, $\rho \approx 1$ means green- and red-labeled containing molecular complexes are overlapping, $\rho \approx 0$ means a random distribution and a value approaching − 1 would mean exclusion. For the Pearson's analysis, the same data as for fluctuation analysis were used, which contains significant shot noise. We, therefore, made an average of the first five image frames to obtain the most reliable Pearson's correlation analysis (Fig. S4H).

TICS and dual-color TICS

Sample preparation and TIRF image series recording was performed as described for the Pearson's co-localization analysis. In each pixel the time series are preprocessed to remove the frame-to-frame variation of intensity using [44] as follows:

$$I_{\mathrm{TICS}}(x,y,t) = I(x,y,t) - \langle I(t)\rangle_{XY} + \langle I\rangle_{XY}, \tag{9}$$

where $I(x,y,t)$ is the intensity of any pixel, $\langle I(t)\rangle_{XY}$ is the mean intensity of frame t and $\langle I\rangle_{XY}$ is the mean intensity over all frames. The region inside the cell membrane was selected via freehand-drawing. To exclude high-intensity clusters either dynamic (as described above for RICS) or static image masking was applied (Videos S3–S5). For static region-of-interest (ROI) selection thresholding occurred based on the average intensity of the whole time series. The intensity threshold was determined empirically to exclude all clusters and regions of significantly higher intensity than the mean intensity of all included pixels in the total

preprocessed (Eq. 9) image series. Pixel-based auto- and cross-correlations were calculated using a one-dimensional discrete Fourier transform algorithm [43, 54] as follows:

$$G(x,y,\tau)=\frac{\langle \delta I_{\mathrm{TICS},1}(x,y,t)\cdot \delta I_{\mathrm{TICS},2}(x,y,t+\tau)\rangle}{\langle I_{\mathrm{TICS},1}(x,y)\rangle\langle I_{\mathrm{TICS},2}(x,y)\rangle}, \tag{10}$$

where τ is the time lag and $\delta I_{\mathrm{TICS},1}=\delta I_{\mathrm{TICS},2}$ for autocorrelation of a single imaging channel, while for dual-color cross-correlation $\delta I_{\mathrm{TICS},1}$ and $\delta I_{\mathrm{TICS},2}$ are the values from the green and red image, respectively. Finally, a one-component model for 2D diffusion was fitted to the autocorrelation functions (ACFs) and cross-correlation function (CCF) to obtain for each fit the average apparent diffusion constant [81]:

$$G_{\mathrm{TICS}}(\tau)=A_D\left(1+\frac{4D\tau}{\omega_r^2}\right)^{-1}+A_0, \tag{11}$$

where A_D is the amplitude of the decaying part of the correlation function, ω_r is the radial waist of the point spread function (PSF) inherent to the resolution of the used microscope (Fig. S5A) and A_0 is the offset caused by, e.g. immobile molecules. It needs to be stated that a fit model, that explicitly takes into account the non-negligible pixel size, and uniform lateral intensity distribution in the case of TIRF excitation (e.g., Eq. 4 from [82]), would lead to more accurate values for D. To avoid influence of very slow motion (e.g. cell drift), the data were fitted until a 12-frame lag (i.e., ~ 1 s). In control experiments we could show that TICS is indeed able to describe slow membrane diffusion (Fig. S4I), while conversely, diffusion of cytosolic eGFP was too fast to be captured via TICS, even at the fastest possible frame rate of the detection system (Fig. S4J). The relative cross-correlation was obtained by dividing the amplitude of the cross-correlation function at the center by the mean of the two amplitudes of the corresponding autocorrelation functions.

$$\mathrm{Rel.CC}=\frac{G_{\mathrm{fit,CCF}}(0)}{\left(G_{\mathrm{fit,ACF1}}(0)+G_{\mathrm{fit,ACF2}}(0)\right)/2}. \tag{12}$$

Whole-cell patch-clamp electrophysiology

Cells were transfected with either GlyR-α3L-eGFP, GlyR-α3K-eGFP or GlyR-α3K-mCherry. Recordings were performed at room temperature in voltage-clamp mode using a HEKA EPC10 amplifier (HEKA Electronics, Lambrecht, Germany) controlled by HEKA acquisition software. Patch pipettes (3–4 MΩ) were filled with internal solution containing 120 mM CsCl, 2 mM Na_2ATP, 2 mM MgATP, 10 mM EGTA and 10 mM HEPES, adjusted to pH 7.2 with CsOH. The standard external solution (SES) had a composition of 150 mM NaCl, 5.4 mM KCl, 2 mM $CaCl_2$, 1 mM $MgCl_2$, 10 mM glucose and 10 mM HEPES. Glycinergic currents were recorded at a holding potential $V_H = -60$mV. Different glycine concentrations in SES including 20 µM, 50 µM, 100 µM, 200 µM, and 500 µM were applied for 10 s. For dose–response curves in whole cell configuration, glycine was applied using a Warner SF77B fast step superfusion system that allowed an exchange time of < 20 ms (Warner Instruments LLC, Hamden, CT, USA). Maximum current amplitude was measured using FitMaster software (HEKA Electronics). The EC_{50} was calculated by plotting the normalized current as a function of concentration and fitting the data with the Hill equation (GraphPad Prism, La Jolla, CA, USA). For desensitization analysis, the decaying current phase was fitted using a mono-exponential in FitMaster software (HEKA Electronics, Lambrecht, Germany).

Cell-attached single-channel electrophysiology

Cells were transfected with either GlyR-α3L-FP, GlyR-α3K-FP or both GlyR-α3L-FP and GlyR-α3K-FP (FP = eGFP or mCherry). Cell-attached recordings were performed in voltage clamp mode at RT using a HEKA EPC10 amplifier with a 2.9-kHz low-pass hardware filter. The external solution contained 120 mM NaCl, 4.7 mM KCl, 2 mM CaCl2, 1.2 mM $MgCl_2$, 10 mM HEPES, 14 mM glucose, 20 mM TEA-Cl, 15 mM sucrose, adjusted to a pH of 7.4 with NaOH. Patch pipettes (5–15 MΩ) were filled with external solution and 30–80 µM glycine. The holding potential was set at 60 mV. Analysis of cell-attached recordings was done using the FitMaster software. Recordings were additionally filtered with a digital 100-Hz low-pass Gaussian filter, that removed the high overall noise but preserved the mean current values used for data interpretation (Fig. S7). Because it was difficult to find proper cells to perform single-channel recordings, different datasets were pooled during analysis: the K-group, therefore, consists of both GlyR-α3K-eGFP (4 cells) and GlyR-α3K-mCherry (21 cells); the L-group consists of both GlyR-α3L-eGFP (18 cells) and GlyR-α3L-mCherry (5 cells). The K/L group consists only of cells expressing GlyR-α3L-eGFP and GlyR-α3K-mCherry. Amplitude histograms from single-channel openings were made by manually selecting short (< 1 s) time windows with single-channel opening events around a constant baseline. Histograms were fit with a Gaussian model yielding the mean open current for the selected time window. Similar currents from a given cell were averaged. A one-way ANOVA and Tukey's multiple comparisons was used to determine significant differences.

Summary of the supplemental material

Fig. S1 shows the immunocytochemistry of the FP tagged GlyR. Fig. S2 shows the combined fluorescence-electrophysiology setup. Fig. S3 illustrates the functional assessment of fluorescent protein tagged GlyR via whole-cell electrophysiology. Fig. S4 shows additional and control image correlation spectroscopy experiments. Fig. S5 shows focus size determination measurements of the Zeiss Elyra PS.1 and LSM880 microscopes. Fig. S6 shows outside-out electrophysiology. Fig. S7 shows the effect of digital filtering of electrophysiology data. Fig. S8 shows the intensity-dependence of fluctuation experiments. The supplementary tables include diffusion constants of the GlyR with frame-based thresholding (Table S1) and with average intensity-based thresholding (Table S2). Table S3 gives Pearson's correlation coefficients to determine co-localization of GlyR-α3L and GlyR-α3K. Parameters obtained from the bleaching histograms fits are shown in Table S4. Brightness of eGFP tagged proteins can be found in Table S5. Video S1-2 correspond to the RICS data presented in Fig. 1E. Video S3-5 are comparisons of the different masking procedures used for TICS analysis. Finally, a discussion on the used fit model for TICS analysis is included.

Supplementary Information The online version contains supplementary material available at https://doi.org/10.1007/s00018-022-04506-9.

Acknowledgements We are greatly indebted to Mrs. Petra Bex for expert assistance with electrophysiology and to Dr. Sam Duwé and Ms. Keerthana Ramanathan for expert assistance with the microscopy. Prof. Em. Marcel Ameloot is thanked for critically reviewing the manuscript. Prof. Gonzalo E. Yevenes and Prof. Gustavo Morage-Cid (Department of Physiology, Faculty of Biological Sciences, University of Concepción, Concepción, Chile) are thanked for constructive discussions on the patch clamp experiments. Supervised students Hanneke Schroyen, Mahnoor Arif, Sam Vanspauwen and Jolien Broekmans are acknowledged for assistance in conducting experiments.

Author contributions Conceptualization JCM, BB and JH; Investigation and formal analysis VL, BT, YV, SK, JL; Software development JH; Writing the original draft VL, BT and JH; Review and editing by all authors.

Funding Open Access funding enabled and organized by Projekt DEAL. J.C. Meier acknowledges the Deutsche Forschungsgemeinschaft DFG (SPP1784, ME2075/7-1) and the Volkswagenstiftung (HOMEO-HIRN, ZN3673) for financial support of doctoral students SK and JL, respectively. We acknowledge the UHasselt Advanced Optical Microscopy Centre (AOMC). Prof. Em. Marcel Ameloot, the Research Foundation Flanders (FWO, project G0H3716N) and the province of Limburg (Belgium) (tUL Impuls II) are acknowledged for funding the microscopy hardware. V. Lemmens is grateful for a doctoral scholarship from the UHasselt (17DOC11BOF) and KU Leuven (C14/16/053) Special Research Fund (BOF). J. Hendrix acknowledges the UHasselt BOF (BOF20TT06).

Availability of data and material All data and material are available upon request.

Code availability Fluctuation imaging and co-localization analyses were performed in the software package PAM (Schrimpf et al., 2018, Biophysical Journal). The software is available as source code, requiring MATLAB to run, or as pre-compiled standalone distributions for Windows or MacOS at http://www.cup.uni-muenchen.de/pc/lamb/software/pam.html or hosted in Git repositories under http://www.gitlab.com/PAM-PIE/PAM and http://www.gitlab.com/PAM-PIE/PAMcompiled. A detailed user manual is available at http://pam.readthedocs.io.

Declarations

Conflict of interest The authors declare that they have no conflicts of interest apply.

Ethical approval Not applicable.

References

1. Dutertre S, Becker C-M, Betz H (2012) Inhibitory Glycine receptors: an update. J Biol Chem 287(48):40216–40223
2. Lynch JW, Zhang Y, Talwar S, Estrada-Mondragon A (2017) Glycine Receptor Drug Discovery. Advances in Pharmacology. Elsevier, pp 225–253
3. Nikolic Z, Laube B, Weber RG, Lichter P, Kioschis P, Poustka A et al (1998) The human glycine receptor subunit α3. J Biol Chem 273(31):19708–19714
4. Uhlén M, Fagerberg L, Hallström BM, Lindskog C, Oksvold P, Mardinoglu A et al (2015) Tissue-based map of the human proteome. Science. https://doi.org/10.1126/science.1260419
5. Eichler S, Förstera B, Smolinsky B, Jüttner R, Lehmann T-N, Fähling M et al (2009) Splice-specific roles of glycine receptor a3 in the hippocampus. Eur J Neurosci 30:1077–1091
6. Çaliskan G, Müller I, Semtner M, Winkelmann A, Raza AS, Hollnagel JO et al (2016) Identification of parvalbumin interneurons as cellular substrate of fear memory persistence. Cereb Cortex 26(5):2325–2340. https://doi.org/10.1093/cercor/bhw001
7. Eichler SA, Kirischuk S, Jüttner R, Schaefermeier PK, Schafermeier PK, Legendre P et al (2008) Glycinergic tonic inhibition of hippocampal neurons with depolarizing GABAergic transmission elicits histopathological signs of temporal lobe epilepsy. J Cell Mol Med 12(6B):2848–2866. https://doi.org/10.1111/j.1582-4934.2008.00357.x
8. Winkelmann A, Maggio N, Eller J, Callskan G, Semtner M, Häussler U et al (2014) Changes in neural network homeostasis trigger neuropsychiatric symptoms. J Clin Investig 124:696–711
9. Harvey RJ, Depner UB, Wässle H, Ahmadi S, Heindl C, Reinold H et al (2004) GlyR α3: an essential target for spinal PGE_2-mediated inflammatory pain sensitization. Science 304:884–887

10. Malosio ML, Grenningloh G, Kuhse J, Schmieden V, Schmitt B, Prior P et al (1991) Alternative splicing generates two variants of the alpha 1 subunit of the inhibitory glycine receptor. J Biol Chem 266(4):2048–2053
11. Kuhse J, Kuryatov A, Maulet Y, Malosio M, Schmieden V, Betz H (1991) Alternative splicing generates two isoforms of the α2 subunit of the inhibitory glycine receptor. FEBS Lett 283(1):73–77
12. Oertel J, Villmann C, Kettenmann H, Kirchhoff F, Becker C-M (2007) A novel glycine receptor β subunit splice variant predicts an unorthodox transmembrane topology assembly into heteromeric receptor complexes. J Biol Chem 282(5):2798–2807
13. Zhang L-H, Gong N, Fei D, Xu L, Xu T-L (2008) Glycine uptake regulates hippocampal network activity via glycine receptor-mediated tonic inhibition. Neuropsychopharmacology 33(3):701–711
14. Meier JC, Semtner M, Winkelmann A, Wolfart J (2014) Presynaptic mechanisms of neuronal plasticity and their role in epilepsy. Front Cell Neurosci 8:164
15. Waseem TV, Fedorovich SV (2010) Presynaptic glycine receptors influence plasma membrane potential and glutamate release. Neurochem Res 35(8):1188–1195
16. Kubota H, Alle H, Betz H, Geiger JR (2010) Presynaptic glycine receptors on hippocampal mossy fibers. Biochem Biophys Res Commun 393(4):587–591
17. Ruiz A, Campanac E, Scott RS, Rusakov DA, Kullmann DM (2010) Presynaptic GABA A receptors enhance transmission and LTP induction at hippocampal mossy fiber synapses. Nat Neurosci 13(4):431
18. Prior P, Schmitt B, Grenningloh G, Pribilla I, Multhaup G, Beyreuther K et al (1992) Primary structure and alternative splice variants of gephyrin, a putative glycine receptor-tubulin linker protein. Neuron 8(6):1161–1170
19. Meyer G, Kirsch J, Betz H, Langosch D (1995) Identification of a gephyrin binding motif on the glycine receptor β subunit. Neuron 15(3):563–572
20. Notelaers K, Smisdom N, Rocha S, Janssen D, Meier JC, Rigo J-M et al (2012) Ensemble and single particle fluorimetric techniques in concerted action to study the diffusion and aggregation of the glycine receptor α3 isoforms in the cell plasma membrane. Biochem Biophys Acta 1818:3131–3140
21. Notelaers K, Rocha S, Paesen R, Smisdom N, De Clercq B, Meier JC et al (2014) Analysis of α3 GlyR single particle tracking in the cell membrane. Biochemica et Biophysica Acta 1843:544–553
22. Notelaers K, Rocha S, Paesen R, Swinnen N, Vangindertael J, Meier JC et al (2014) Membrane distribution of the glycine receptor α3 studied by optical super-resolution microscopy. Histochem Cell Biol 142:79–90
23. Patrizio A, Renner M, Pizzarelli R, Triller A, Specht C (2017) Alpha subunit-dependent glycine receptor clustering and regulation of synaptic receptor numbers. Sci Rep 7(1):1–11
24. Marabelli A, Moroni M, Lape R, Sivilotti LG (2013) The kinetic properties of the α3 rat glycine receptor make it suitable for mediating fast synaptic inhibition. J Physiol 591(13):3289–3308
25. Breitinger HG, Villmann C, Rennert J, Ballhausen D, Becker CM (2002) Hydroxylated residues influence desensitization behaviour of recombinant α3 glycine receptor channels. J Neurochem 83(1):30–36
26. Acuña MA, Yévenes GE, Ralvenius WT, Benke D, Di Lio A, Lara CO et al (2016) Phosphorylation state-dependent modulation of spinal glycine receptors alleviates inflammatory pain. J Clin Investig 126(7):2547–2560
27. Lara CO, Murath P, Muñoz B, Marileo AM, San Martín L, San Martín VP et al (2016) Functional modulation of glycine receptors by the alkaloid gelsemine. Br J Pharmacol 173(14):2263–2277
28. Moraga-Cid G, San Martín VP, Lara CO, Muñoz B, Marileo AM, Sazo A et al (2020) Modulation of glycine receptor single-channel conductance by intracellular phosphorylation. Sci Rep 10(1):1–11
29. Bormann J, Rundström N, Betz H, Langosch D (1993) Residues within transmembrane segment M2 determine chloride conductance of glycine receptor homo-and hetero-oligomers. EMBO J 12(10):3729–3737
30. Carland JE, Cooper MA, Sugiharto S, Jeong HJ, Lewis TM, Barry PH et al (2009) Characterization of the effects of charged residues in the intracellular loop on ion permeation in α1 glycine receptor channels. J Biol Chem 284(4):2023–2030. https://doi.org/10.1074/jbc.M806618200
31. Schwille P, Meyer-Almes F-J, Rigler R (1997) Dual-color fluorescence cross-correlation spectroscopy for multicomponent diffusional analysis in solution. Biophys J 72(4):1878–1886
32. Digman MA, Wiseman PW, Horwitz AR, Gratton E (2009) Detecting protein complexes in living cells from laser scanning confocal image sequences by the cross correlation raster image spectroscopy method. Biophys J 96(2):707–716
33. McGuire H, Aurousseau MR, Bowie D, Blunck R (2012) Automating single subunit counting of membrane proteins in mammalian cells. J Biol Chem 287(43):35912–35921
34. Ulbrich MH, Isacoff EY (2007) Subunit counting in membrane-bound proteins. Nat Methods 4(4):319–321
35. Notelaers K, Smisdom N, Rocha S, Janssen D, Meier JC, Rigo J-M et al (2012) Ensemble and single particle fluorimetric techniques in concerted action to study the diffusion and aggregation of the glycine receptor α3 isoforms in the cell plasma membrane. Biochem Biophys Acta 1818(12):3131–3140. https://doi.org/10.1016/j.bbamem.2012.08.010
36. David-Watine B, Goblet C, de Saint JD, Fucile S, Devignot V, Bregestovski P et al (1999) Cloning, expression and electrophysiological characterization of glycine receptor alpha subunit from zebrafish. Neuroscience 90(1):303–317
37. Watanabe N, Mitchison TJ (2002) Single-molecule speckle analysis of actin filament turnover in lamellipodia. Science 295(5557):1083–1086
38. Groot-Kormelink PJ, Beato M, Finotti C, Harvey RJ, Sivilotti LG (2002) Achieving optimal expression for single channel recording: a plasmid ratio approach to the expression of α1 glycine receptors in HEK293 cells. J Neurosci Methods 113(2):207–214
39. Wong K, Briddon SJ, Holliday ND, Kerr ID (2016) Plasma membrane dynamics and tetrameric organisation of ABCG2 transporters in mammalian cells revealed by single particle imaging techniques. Biochimica et Biophysica Acta (BBA) 1863(1):19–29
40. Brown C, Dalal R, Hebert B, Digman M, Horwitz A, Gratton E (2008) Raster image correlation spectroscopy (RICS) for measuring fast protein dynamics and concentrations with a commercial laser scanning confocal microscope. J Microsc 229(1):78–91
41. Digman MA, Brown CM, Sengupta P, Wiseman PW, Horwitz AR, Gratton E (2005) Measuring fast dynamics in solutions and cells with a laser scanning microscope. Biophys J 89(2):1317–1327
42. Digman MA, Sengupta P, Wiseman PW, Brown CM, Horwitz AR, Gratton E (2005) Fluctuation correlation spectroscopy with a laser-scanning microscope: exploiting the hidden time structure. Biophys J 88(5):L33–L36
43. Wiseman P, Squier J, Ellisman M, Wilson K (2000) Two-photon image correlation spectroscopy and image cross-correlation spectroscopy. J Microsc 200(1):14–25
44. Hendrix J, Baumgärtel V, Schrimpf W, Ivanchenko S, Digman MA, Gratton E et al (2015) Live-cell observation of cytosolic HIV-1 assembly onset reveals RNA-interacting Gag oligomers. J Cell Biol 210(4):629–649
45. Longfils M, Smisdom N, Ameloot M, Rudemo M, Lemmens V, Fernández GS et al (2019) Raster image correlation spectroscopy performance evaluation. Biophys J 117(10):1900–1914

46. Kolin DL, Costantino S, Wiseman PW (2006) Sampling effects, noise, and photobleaching in temporal image correlation spectroscopy. Biophys J 90(2):628–639
47. Manders E, Stap J, Brakenhoff G, Van Driel R, Aten J (1992) Dynamics of three-dimensional replication patterns during the S-phase, analysed by double labelling of DNA and confocal microscopy. J Cell Sci 103(3):857–862
48. Bolte S, Cordelières FP (2006) A guided tour into subcellular colocalization analysis in light microscopy. J Microsc 224(3):213–232
49. Dunn KW, Kamocka MM, McDonald JH (2011) A practical guide to evaluating colocalization in biological microscopy. Am J Physiol Cell Physiol 300(4):C723–C742
50. Hendrix J, Gijsbers R, De Rijck J, Voet A, Hotta J-I, McNeely M et al (2011) The transcriptional co-activator LEDGF/p75 displays a dynamic scan-and-lock mechanism for chromatin tethering. Nucleic acids Res 39(4):1310–1325
51. Schrimpf W, Lemmens V, Smisdom N, Ameloot M, Lamb DC, Hendrix J (2018) Crosstalk-free multicolor RICS using spectral weighting. Methods 140:97–111
52. Calebiro D, Rieken F, Wagner J, Sungkaworn T, Zabel U, Borzi A et al (2013) Single-molecule analysis of fluorescently labeled G-protein–coupled receptors reveals complexes with distinct dynamics and organization. Proc Natl Acad Sci 110(2):743–748
53. Işbilir A, Möller J, Arimont M, Bobkov V, Perpiñá-Viciano C, Hoffmann C et al (2020) Advanced fluorescence microscopy reveals disruption of dynamic CXCR4 dimerization by subpocket-specific inverse agonists. Proc Natl Acad Sci 117(46):29144–29154
54. Srivastava M, Petersen NO (1998) Diffusion of transferrin receptor clusters. Biophys Chem 75(3):201–211
55. Hendrix J, Dekens T, Schrimpf W, Lamb DC (2016) Arbitrary-region raster image correlation spectroscopy. Biophys J 111:1–12
56. Fogarty KH, Chen Y, Grigsby IF, Macdonald PJ, Smith EM, Johnson JL et al (2011) Characterization of cytoplasmic Gag-gag interactions by dual-color z-scan fluorescence fluctuation spectroscopy. Biophys J 100(6):1587–1595
57. Vercammen J, Maertens G, Gerard M, De Clercq E, Debyser Z, Engelborghs Y (2002) DNA-induced polymerization of HIV-1 integrase analyzed with fluorescence fluctuation spectroscopy. J Biol Chem 277(41):38045–38052
58. Lemmens V, Ramanathan K, Hendrix J (2020) Fluorescence microscopy data for quantitative mobility and interaction analysis of proteins in living cells. Data Brief 29:105348
59. Gambin Y, Lopez-Esparza R, Reffay M, Sierecki E, Gov N, Genest M et al (2006) Lateral mobility of proteins in liquid membranes revisited. Proc Natl Acad Sci 103(7):2098–2102
60. Weiß K, Neef A, Van Q, Kramer S, Gregor I, Enderlein J (2013) Quantifying the diffusion of membrane proteins and peptides in black lipid membranes with 2-focus fluorescence correlation spectroscopy. Biophys J 105(2):455–462. https://doi.org/10.1016/j.bpj.2013.06.004
61. Choquet D (2010) Fast AMPAR trafficking for a high-frequency synaptic transmission. Eur J Neurosci 32(2):250–260
62. Weltzien F, Puller C, O'Sullivan GA, Paarmann I, Betz H (2012) Distribution of the glycine receptor β-subunit in the mouse CNS as revealed by a novel monoclonal antibody. J Comp Neurol 520(17):3962–3981
63. Meier J, Grantyn R (2004) A gephyrin-related mechanism restraining glycine receptor anchoring at GABAergic synapses. J Neurosci 24(6):1398–1405
64. Durisic N, Godin AG, Wever CM, Heyes CD, Lakadamyali M, Dent JA (2012) Stoichiometry of the Human Glycine receptor revealed by direct subunit counting. J Neurosci 32:12915–12920
65. Schaefer N, Roemer V, Janzen D, Villmann C (2018) Impaired Glycine receptor trafficking in neurological diseases. Front Mol Neurosci 11:291
66. van Steensel B, van Binnendijk EP, Hornsby CD, Van der Voort H, Krozowski ZS, de Kloet ER et al (1996) Partial colocalization of glucocorticoid and mineralocorticoid receptors in discrete compartments in nuclei of rat hippocampus neurons. J Cell Sci 109(4):787–792
67. Förstera B, Dzaye OD, Winkelmann A, Semtner M, Benedetti B, Markovic DS et al (2014) Intracellular glycine receptor function facilitates glioma formation in vivo. J Cell Sci 127(17):3687–3698
68. Kluba M, Engelborghs Y, Hofkens J, Mizuno H (2015) Inhibition of receptor dimerization as a novel negative feedback mechanism of EGFR signaling. PLoS One 10(10):e0139971
69. Pack C, Saito K, Tamura M, Kinjo M (2006) Microenvironment and effect of energy depletion in the nucleus analyzed by mobility of multiple oligomeric EGFPs. Biophys J 91(10):3921–3936
70. Chen C, Okayama H (1987) High-efficiency transformation of mammalian cells by plasmid DNA. Mol Cell Biol 7(8):2745–2752
71. Liebsch F, Aurousseau MR, Bethge T, McGuire H, Scolari S, Herrmann A et al (2017) Full-length cellular β-secretase has a trimeric subunit stoichiometry, and its sulfur-rich transmembrane interaction site modulates cytosolic copper compartmentalization. J Biol Chem 292(32):13258–13270
72. Dunsing V, Luckner M, Zühlke B, Petazzi RA, Herrmann A, Chiantia S (2018) Optimal fluorescent protein tags for quantifying protein oligomerization in living cells. Sci Rep 8(1):1–12
73. Godin AG, Rappaz B, Potvin-Trottier L, Kennedy TE, De Koninck Y, Wiseman PW (2015) Spatial intensity distribution analysis reveals abnormal oligomerization of proteins in single cells. Biophys J 109(4):710–721
74. Arant RJ, Ulbrich MH (2014) Deciphering the subunit composition of multimeric proteins by counting photobleaching steps. ChemPhysChem 15(4):600–605
75. Hines KE (2013) Inferring subunit stoichiometry from single molecule photobleaching. J Gen Physiol 141(6):737–746
76. Schrimpf W, Barth A, Hendrix J, Lamb DC (2018) PAM: a framework for integrated analysis of imaging, single-molecule, and ensemble fluorescence data. Biophys J 114(7):1518–1528
77. Mets RD, Delon A, Balland M, Destaing O, Wang I (2020) Dynamic range and background filtering in raster image correlation spectroscopy. J Microscopy 279(2):123–138. https://doi.org/10.1111/jmi.12925
78. Ivanchenko S, Lamb DC (2011) Fluorescence correlation spectroscopy: principles and developments. Supramolecular Structure and Function 10. Springer, Dordrecht, pp 1–30
79. Comeau JW, Costantino S, Wiseman PW (2006) A guide to accurate fluorescence microscopy colocalization measurements. Biophys J 91(12):4611–4622. https://doi.org/10.1529/biophysj.106.089441
80. Oneto M, Scipioni L, Sarmento MJ, Cainero I, Pelicci S, Furia L et al (2019) Nanoscale distribution of nuclear sites by super-resolved image cross-correlation spectroscopy. Biophys J 117(11):2054–2065. https://doi.org/10.1016/j.bpj.2019.10.036
81. Kannan B, Guo L, Sudhaharan T, Ahmed S, Maruyama I, Wohland T (2007) Spatially resolved total internal reflection fluorescence correlation microscopy using an electron multiplying charge-coupled device camera. Anal Chem 79(12):4463–4470. https://doi.org/10.1021/ac0624546
82. Guo L, Har JY, Sankaran J, Hong Y, Kannan B, Wohland T (2008) Molecular diffusion measurement in lipid bilayers over wide concentration ranges: a comparative study. ChemPhysChem 9(5):721–728. https://doi.org/10.1002/cphc.200700611